JSWSC

RESEARCH ARTICLE   **OPEN ∂ ACCESS**

Interhemispheric variability of the electron density and derived parameters by the Swarm satellites during different solar activity

Daria Kotova*, Yaqi Jin, and Wojciech Miloch

Department of Physics, University of Oslo, Box 1048 Blindern, 0316 Oslo, Norway

Abstract – With the data from the Swarm satellite mission, we study the variability of ionospheric plasma parameters for low and high solar activities. We focus on the electron density measured by Swarm and derived parameters and analyze the variability of these parameters in the contexts of the Northern and Southern hemispheres, specific latitudinal regions, and the solar activity level. We consider two time intervals: with high solar activity (HSA) from August 2014 to July 2015 and with low solar activity (LSA) from January to December 2018. We show that the electron density is described mainly by three probability density functions (PDF): exponentiated Weibull, lognormal, and chi distributions. These results with PDFs can be applied to the modeling or prediction of ionospheric parameters in different regions. The best fit of PDFs was obtained for low and mid-latitudes, while at high latitudes and in the polar caps, the double-peaked features of the distribution require the fit of multiple PDFs. The electron density (Ne) distribution at low latitudes follows more a lognormal distribution, while in the high latitude region, the chi distribution prevails. Different results were obtained for the rate of change of density index (RODI) with two fitting PDFs: lognormal or exponentiated Weibull, where the best fits are for high latitudes and polar caps. We demonstrate high variability in the electron density and derived parameters at low latitudes and in the polar caps. Comparing both hemispheres, we obtained higher values of these parameters during the solar minimum in the Southern hemisphere at high latitudes and polar caps, while for the Northern hemisphere, higher values were obtained at low latitudes. The dependence on the satellite's altitude was also considered. The main patterns in the diurnal variation of parameters in different regions do not depend on the level of solar activity (which affects only the maximum values). The largest asymmetry between both hemispheres in Ne diurnal distribution was obtained for the polar cap regions. Here a 50% decrease in Ne was observed in the Northern hemisphere during HSA in the early morning sector (04–07 Magnetic Local Time), which has not yet been observed in the Southern hemisphere. For the first time, such a global statistical characterization of the ionospheric plasma density based on the in situ data is presented.

Keywords: global statistical study / variability of electron density / symmetry and asymmetry Northern and Southern hemispheres / probability density functions of Ne / diurnal variation of ionosphere

1 Introduction

Various ground-based instruments for ionospheric monitoring (such as ionosondes, radars, Global Navigation Satellite System (GNSS) receivers, and others) have limited coverage. The use of satellite data allows us to study the variability of ionospheric plasma parameters globally, including oceans and inaccessible polar regions, without the need to refer to ground-based instrumentation. The launch of satellites with scientific payload started a new epoch for investigations of the processes taking place in the ionosphere and magnetosphere. While initially most of the papers were related to the case

studies (e.g., Dyson et al., 1974; Cerisier et al., 1985; Basu et al., 1988, 1990), with the advent of polar-orbiting satellites, as well as due to the accumulation of sufficient amount of data, it became possible to conduct global studies. With data from various satellite missions (e.g., DEMETER, COSMIC, FORMOSAT, NorSat-1, Intercosmos-19, ICON, CHAMP, GRACE, Swarm, DMSP, AMPERE, TIMED, CSES, etc.), ionospheric studies were carried out in both global and local contexts. Examples of recent studies of the ionosphere using the low earth orbit (LEO) satellites are Spicher et al. (2017), Jin et al. (2019, 2020), Aa et al. (2020), Chernyshov et al. (2020), Spogli et al. (2020), Yang et al. (2020) or Zhang et al. (2021).

Satellite data can also be successfully used to study interhemispheric differences in the ionospheric response to

---

*Corresponding author: dariakot@fys.uio.no

geomagnetic activity. Laundal & Østgaard (2009) used images from two satellites that could observe the location of aurora in both hemispheres at the same time. They found a case where the aurora was completely asymmetric: during the Northern summer (Southern winter), there was dawn aurora in the Northern hemisphere (NH) and dusk aurora in the Southern hemisphere (SH). Østgaard et al. (2011) used auroral images from satellites to study how the orientation of the interplanetary magnetic field (IMF) affected the location of the substorm onset in both hemispheres. Their study shows how the average substorm locations are related to IMF B_y component. The relation is not linear and reveals a saturation effect for positive (negative) B_y values in the NH (SH). At $B_y < 0$, the substorm occurs earlier in the evening in the NH than in the SH, and the opposite is valid for $B_y > 0$. The asymmetry between the hemispheres is greatest when the clock angle (an angle between the IMF and Z-axis in the YZ plane of the Geocentric Solar Magnetospheric reference system) is $\theta_c = 90°$ and $\theta_c = 270°$.

The launch of the European Space Agency's Swarm constellation mission made it possible to carry out a number of studies of the ionosphere focusing on such aspects as the electric and magnetic fields or plasma temperature, structuring, and irregularities (Friis-Christensen et al., 2008, https://earth.esa.int/web/guest/missions/esa-eo-missions/swarm/activities/publications). The Swarm satellites have also been used to compare the polar ionosphere in the NH and the SH. Spicher et al. (2017) studied the occurrence of the polar cap patches (PCPs) using the Swarm data from December 2013 to August 2016. They found higher occurrences of PCPs in the Antarctic than in the Arctic. In both hemispheres, there were more PCPs during local winter than in summer, and this seasonal variation was stronger in the Arctic. For $B_y < 0$, there were more PCPs in the NH afternoon, while for $B_y > 0$, there were more before noon. This effect was the opposite in the SH.

Jin et al. (2019) used data from the Swarm satellites to study the electron density and its variations over the Arctic and Antarctic, with a time series from 2014 to 2019. This study revealed that the irregularities are mostly in the dayside cusp, polar cap, and the night side of the auroral oval. With IMF $B_y < 0$, in the polar cap and cusp, strong irregularities occurred in the dusk in the NH and the dawn in the SH. The seasonal variations in the irregularity level were more pronounced in the Antarctic than in the Arctic. In the Antarctic, the strongest irregularities were observed in December (local summer), while in the Arctic, they were strongest between April to September, with a local minimum during local summer. The authors also found more irregularities during the solar maximum. Further study by Jin et al. (2020) presented global climatological distributions of ionospheric plasma irregularities and confirmed three main regions of strong ionospheric irregularities: the magnetic equator extending from postsunset to early morning, the auroral ovals (from dayside cusp to nightside auroral oval), and within the polar caps. Based on Swarm data, Jin & Xiong (2020) presented an interhemispheric study of the large-scale (100 km) density gradients in both polar caps. These gradients in the Arctic are enhanced during local winter (December solstice) with a peak around 19 Universal Time (UT), and in the Antarctic local winter (June solstice), the peak is around 07 UT. They found that the only asymmetry (anomaly) is the persistence of strong density gradients in the southern polar cap during local summer (December solstice).

Aa et al. (2020) used the Swarm data to study the main ionospheric trough. They demonstrated a hemispherical asymmetry: during a local winter and equinoxes, the trough is more evident in the NH, with the average nighttime occurrence rate being 20–30% higher than that in the SH. Besides, the trough minimum position and the trough width also exhibit more significant fluctuations in the NH.

Despite the large number of studies conducted, they were mostly focused on particular regions and phenomena, and only a few of them were attempting a global study. A comprehensive, global study of plasma variability based on a large dataset can provide valuable information on the distribution of ionospheric parameters in different latitudinal regions for both hemispheres. Such data will be useful both for verification and construction of empirical and assimilative ionospheric models (e.g., Parameterized Real-Time Ionospheric Specification Model [PRISM], Daniell & Brown, 1995); Global Assimilation of Ionospheric Measurements (GAIM, Schunk et al., 2004); International Reference Ionosphere (IRI, Bilitza & Reinisch, 2008), as well as for the development of new satellite instruments or missions, and contribute to end-to-end simulators for new spacecraft missions (e.g., the Daedalus candidate mission: Sarris et al., 2020; Palmroth et al., 2021). They would also contribute to models for the accuracy and reliability of GNSS precise positioning.

This work provides results from a comprehensive and quantitative study of distributions of parameters derived from the plasma density measurements by Swarm. We show statistics and distributions of selected ionospheric parameters together with the best fits of probability density functions (PDFs), as well as describe and discuss in detail the diurnal variation in the electron density and in the rate of change of density. They are analyzed in the context of geomagnetic latitudinal regions, Northern and Southern hemispheres, levels of solar activity, and the magnetic local time. The analysis of different parameters makes it possible to estimate the contribution of plasma variations with spatial scales ranging from 3 km to 300 km.

2 Approach

The analysis is carried out with data from the Swarm satellites. The Swarm mission is a constellation of three satellites that were launched on 22 November 2013 and had been collecting data continuously since then. After the commission phase, the final constellation of the mission was achieved on 17 April 2014 with the orbital altitudes of Swarm A and C satellites at about 470 km, while the orbit of Swarm B is somewhat higher at 520 km. The payload instrumentation of each of the satellites includes electric field instrument (EFI), vector and absolute scalar field magnetometers, accelerometer, and the global positioning system (GPS) receiver. This study uses data from the plasma density measurements obtained with the Langmuir probe within EFI. A distinctive feature of the Swarm mission is that the satellite trajectories pass over the polar regions and that their orbits slowly process, covering different local times, which allows for studying the physics and dynamics of processes in different ionospheric regions. Each satellite takes about 130 days to cover all local times and about five years to provide the even coverage of local times during all seasons.

A large amount of data gathered over several years allows for statistical studies of both hemispheres overall local times and at different solar and geomagnetic activities. The Swarm data that describe the variability in the ionospheric plasma have been integrated into a unique dataset, called the Ionospheric Plasma IRregularities product (IPIR) and available at https://swarm-diss.eo.esa.int/#swarm/Level2daily/Latest_baselines/IPD/IRR as IPDxIRR_2F (x = A, B or C defining the Swarm satellite). The IPIR dataset contains information about the plasma density, temperature, total electron content (TEC). IPIR defines the plasma variability parameters: rate of change of density (ROD), rate of change of density index (RODI), standard deviation, and electron density gradient. It also assigns the data to geomagnetic regions associated with different physical processes related to the governing ionospheric processes. The equatorial region is defined between ±30° MLAT (geoMagnetic LATitude) in agreement with several previous studies (e.g., Park et al., 2010) and the IBI L2 (Ionospheric Bubble Index) IBIxTMS_2F product (available at https://swarm-diss.eo.esa.int/#swarm%2FLevel2daily%2FLatest_baselines%2FIBI%2FTMS). The mid-latitude region is between ±30° MLAT and equatorward of the Auroral Oval Boundary (AOB, available at https://swarm-diss.eo.esa.int/#swarm%2FLevel2daily%2FLatest_baselines%2FAOB%2FFAC as AOBxFAC_2F product). The extent and location of the auroral oval are dynamic (Kauristie et al., 1999), and AOBs depend on geomagnetic activity. In IPIR, AOBs are defined with the use of the field-aligned current (FAC) method. Estimates of FACs (single satellite method) are routinely derived from the magnetic measurements of each Swarm satellite and provided as the L2 data product FACxTMS_2F (available at https://swarm-diss.eo.esa.int/#swarm/Level2daily/Latest_baselines/FAC/TMS). For determining the auroral boundaries, we use the small-scale (up to 10 km) FAC part of this data product. The polar cap is defined as a region poleward of the auroral oval, or when the poleward boundary of the oval is not found, it is assigned to regions poleward of 77° MLAT, as it was also defined in the polar cap products for Swarm (Spicher et al., 2017).

In this work, the analysis is carried out for the following plasma density (Ne) variability parameters: ROD, RODI in 10 and 20 s (RODI_10s and RODI_20s), filtered Ne fluctuations in 10, 20, and 40 s (delta_Ne10s, delta_Ne20s, delta_Ne40s), Ne gradients at 100, 50, and 20 km scales (Grad_Ne@100km, Grad_Ne@50km, Grad_Ne@20km), and with the electron and background electron densities (Ne and bNe).

ROD is the time derivative of the electron density:

$$\text{ROD}(t) = \frac{Ne(t + \Delta t) - Ne(t)}{\Delta t}. \tag{1}$$

For calculating ROD, we use 2 Hz Swarm Langmuir probe data for accounting for small scale fluctuations about 3–4 km, while all parameters in the IPIR dataset are provided with 1 Hz resolution due to synchronization with other datasets which are also included in IPIR. RODI_10s (RODI_20s) is the standard deviation of ROD in a running window of 10 (20) s:

$$\text{RODI}(t) = \sqrt{\frac{1}{N - 1} \sum_{t_i = t - \Delta t/2}^{t_i = t + \Delta t/2} \left| \text{ROD}(t_i) - \overline{\text{ROD}} \right|^2} \tag{2}$$

where $\overline{\text{ROD}}$ this is the mean of $\text{ROD}(t_i)$ in the respective time interval:

$$\overline{\text{ROD}} = \frac{1}{N} \sqrt{\sum_{t_i = t - \Delta t/2}^{t_i = t + \Delta t/2} \text{ROD}(t_i)}. \tag{3}$$

Filtered electron density parameters, $\Delta Ne10s$, $\Delta Ne20s$, $\Delta Ne40s$, are derived by subtracting the median filtered values in 10, 20, and 40 s from Ne, respectively. Therefore, $\Delta Ne10s$ ($\Delta Ne20s$, $\Delta Ne40s$) indicates electron density fluctuations smaller than 75 km (150 km, 300 km) for Swarm.

The plasma density gradients (∇Ne) Grad_Ne@100km (Grad_Ne@50km, Grad_Ne@20km) are calculated in a running window of 27 (13, 5) data points, which corresponds to the spatial scale of 100 km (50 km, 20 km) for Swarm.

We also calculate the amplitudes of the electron density variations which are defined as a moving standard deviation of $\Delta Ne10s$ chosen in a running window of 10 s. This measure provides the absolute amplitude of fluctuations in plasma over a time interval of 10 s:

$$A(Ne)_{10s}(t) = \sqrt{\frac{1}{N - 1} \sum_{t_i = t - \Delta t/2}^{t_i = t + \Delta t/2} \left| \Delta Ne10s(t_i) - \overline{\Delta Ne10s} \right|^2} \tag{4}$$

where $\overline{\Delta Ne10s}$ is the mean of $\Delta Ne10s(t_i)$:

$$\overline{\Delta Ne10s} = \frac{1}{N} \sum_{t_i = t - \Delta t/2}^{t_i = t + \Delta t/2} \Delta Ne10s(t_i). \tag{5}$$

Given that the velocity of Swarm satellites is about 7.5 km/s and that the resolution of the considered dataset is 1 Hz, the characteristic scales for irregularities are Ne = 7.5 km, ROD = 3–4 km (as ROD is calculated with the 2 Hz dataset), RODI_10s = 75 km, RODI_20s = 150 km, Amplitude = 75 km. To summarize, the IPIR dataset characterizes plasma density fluctuations and irregularities encountered by Swarm in terms of their spatial occurrence, amplitudes, and gradients. More details on the IPIR dataset can be found in (Jin et al., 2022).

We consider two time intervals with respect to the levels of solar activity: (1) high solar activity (HSA) from August 2014 to July 2015 and (2) low solar activity (LSA) from January to December 2018. These periods were chosen based on the solar activity index F10.7, which is the solar radio flux at a wavelength of 10.7 cm (https://omniweb.gsfc.nasa.gov/form/dx1.html). In Supplementary Materials (Fig. SM0), we present the behavior of the solar radio flux index F10.7 in the period from 2010 to 2020 and highlight the intervals with different solar activity levels selected for this study. The data has been divided into four geomagnetic regions in the NH and SH according to IPIR's ionospheric region flag. We used magnetic quasi-dipole latitude (Richmond, 1995; Emmert et al., 2010) to convert from geographic to geomagnetic coordinates.

A threshold of 10^4 cm^{-3} has been used for the electron density (Ne) and background electron density (bNe) to exclude erroneous negative and too small values of the electron density (which are sometimes observed during the solar minimum). bNe is calculated from Ne using a 35th percentile filter of

551 data points (corresponding to approximately 2000 km for 2 Hz data). In addition, in the region of low and mid-latitudes around 09 and 15 magnetic local time (MLT), there have been observed artifacts in the Langmuir probe data from all Swarm satellites. Details on their morphology and occurrence have been given in supplementary material to Jin et al. (2020). To eliminate this artifact in the Langmuir probe data, a filter based on comparison with data obtained with the onboard GPS receiver was used. The following data filtering was used for two time intervals: (1) 8.1 MLT < t < 9.3 MLT; (2) 14.3 MLT < t < 16.0 MLT: if RODI data was larger than 1000 cm^{-3}/s and the rate of change of TEC index (ROTI) was less than 0.02 (0.01) TECU/s, then such data was discarded. A level of 0.02 TECU/s corresponds to the usual distribution of ROTI in 10 s near noise for a high level of solar activity and 0.01 TECU/s for a low one. If a column of the dataset contains NaN values, we discard the rows containing missing values. Thus, after such processing, the length of the arrays for HSA and LSA, as for NH and SH, can be different. Therefore, in the analysis, we will rely more on the value of the parameters when comparing activity levels and hemispheres rather than on the frequency of observation of such a parameter value.

For each hemisphere, we calculate the statistics of the selected plasma parameters (such as Ne, bNe, Amplitude Ne, ΔNe, ROD, RODI, ∇Ne) and quantify their distributions in each of the geomagnetic regions and the considered high and low activity periods. We also analyze in detail the diurnal variations of the parameters (Ne and RODI in 10 s) by focusing on local magnetic time characteristics in respective regions.

3 Results and discussion

3.1 Statistics and distribution of parameters for different regions, hemispheres, and levels of solar activity

We start with presenting results of statistics of all parameters in the context of different regions in both hemispheres for high and low levels of solar activity. Figures 1a–1d present for each of the regions the following statistics of the considered parameters with a box-and-whisker plot: maximum and minimum (the highest and lowest data point in the data set excluding any outliers), median, as well as lower (25%), and upper (75%) quartile percentiles, which indicate that the 25% and 75% of all values are below that percentile value, respectively. Note that outliers are not shown here due to their high values.

To visualize the differences between the regions and both hemispheres, we show in Figure 2a the distribution of electron density, Ne, obtained by Swarm A.

The trends in the electron density distribution can be related to the solar zenith angle, and thus the highest variations are at low latitudes, followed by mid- and higher latitudes. However, there are differences between both hemispheres and, in particular, at higher latitudes. The variations at equatorial latitudes are higher in the NH during both HSA and LSA. This predominance of the NH can be explained by the difference in the position of the geographic and geomagnetic poles, hence the difference in geographic and geomagnetic latitudes. This can lead to differences in sunlight exposure in the two magnetic hemispheres (Laundal et al., 2017). Since the regions for studies

were considered in geomagnetic coordinates, in the low-latitude region in the NH, there are more measurements related to high ionization rate as compared to the SH. Balan et al. (1997) discussed that the neutral wind causes North–South asymmetries in the equatorial plasma fountain and equatorial anomaly due to the displacement of the geomagnetic and geographic equators and the magnetic declination angle.

The SH shows larger variations than NH and the predominance of values of Ne in the high latitude region over the polar cap, meaning there are higher variability and density values observed in the auroral region than in the polar cap in the NH. This is also observed during the solar minimum. Laundal et al. (2017) examined in detail the impact of the North–South asymmetries in Earth's magnetic field and pole offsets on the difference in the solar illumination in both hemispheres. They show that with the effect of the variation in Sun–Earth distance, the polar regions in the SH receive more sunlight during most seasons.

In the NH, both the high latitude region and the polar cap show almost the same distributions, but the higher values are recorded in the polar cap (the mean value of Ne in polar cap with HSA (LSA) is 1.356×10^5 cm^{-3} (0.483×10^5 cm^{-3}) versus 1.263×10^5 cm^{-3} (0.472×10^5 cm^{-3}) in the auroral oval region). The impact of solar activity is significant, and there is more than a two-fold decrease in the maximum values in all regions. These results agree well with the results for the background electron density (see Supplementary Material, SM). The main reason for such a huge difference with maximal value for plasma parameters between HSA and LSA is that solar radiation is subject to considerable variation in intensity during the solar cycle. This is also related to solar flares and coronal mass ejections, which are predominant during HSA. They lead to an increase in geomagnetic activity, enhanced ionization, and the creation of irregular structures in the ionosphere. This is reflected in the distributions of irregularities presented in Figure 2b, which show up to six times higher variations in RODI during HSA as compared to LSA.

Figure 2b presents the distributions of the Rate of change Of Density Index in 10 s, which corresponds to scales up to 75 km. It is seen that for HSA, the variability of RODI in the polar cap is significant, and it is second to the equatorial region. The variability is highest at low latitudes, associated with the equatorial plasma bubbles (Woodman & La Hoz, 1976) and will be discussed in Section 3.3.1. The variability is also significant in the auroral oval and polar caps, and it is lowest at mid-latitudes. This clearly reflects the strong disturbances of the ionosphere in these regions.

Higher latitudes include dynamic phenomena related to the precipitation of charged particles from the Earth's magnetosphere in the auroral oval, as well as formation and structuring of the polar cap patches with scales between 100 and 1000 km (Ren et al., 2018). These processes are more intense during the solar maximum, which is also reflected in the plots. With a declining solar cycle, the observations of PCPs are reduced with respect to the number of patches detected per day, PCP strength, and duration (Dandekar, 2002). In general, the variability decreases not only in the polar cap but also in all other regions (it is lowered by up to 75%). Our results (see Fig. 1d) also concur with the work by Spicher et al. (2017), who showed that the occurrence rate of PCPs observed by Swarm is larger in the SH than in the NH (the upper percentiles for RODI in the NH are
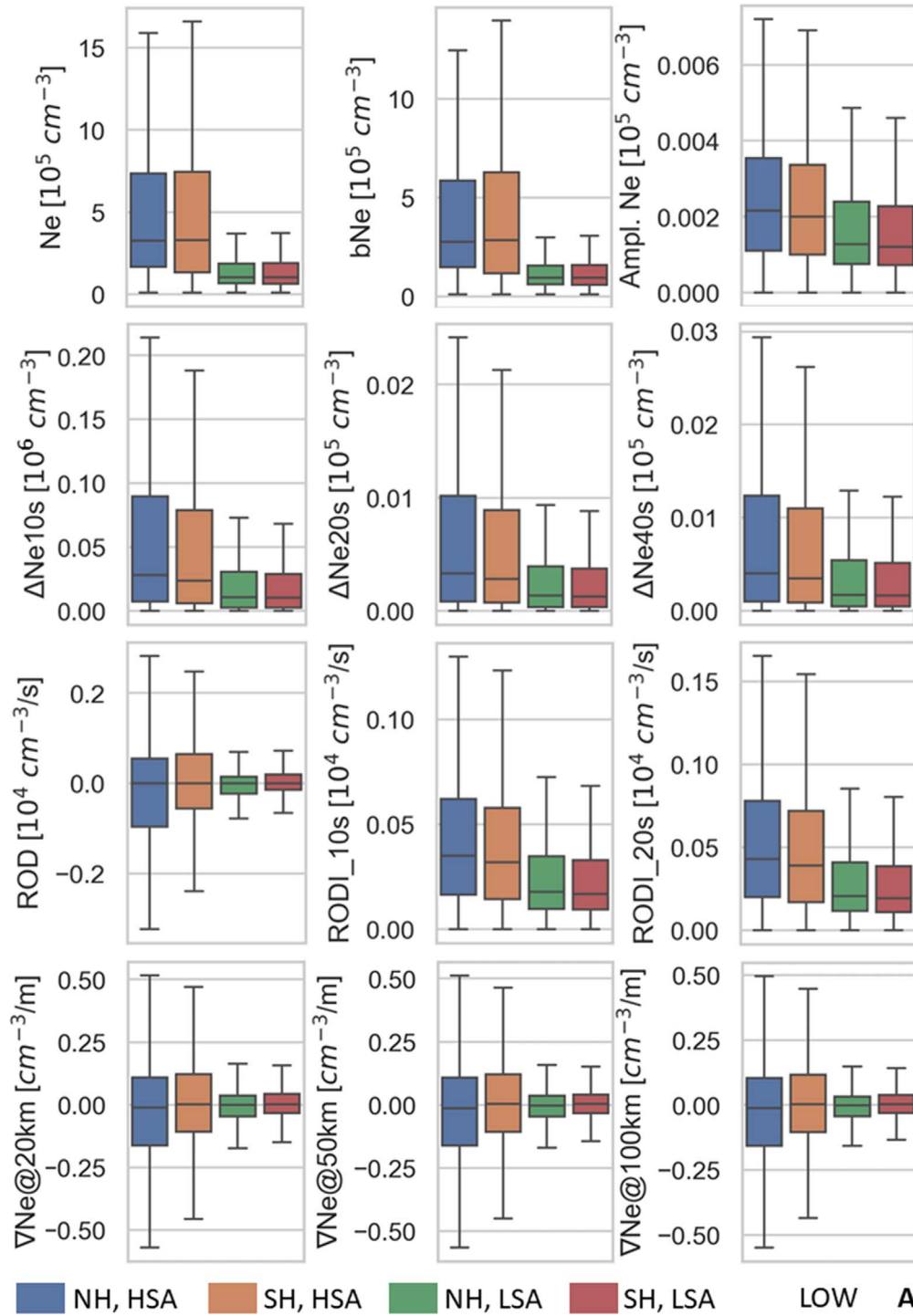
Fig. 1. Box-plot with whiskers of different plasma parameters based on data from Swarm A in the Northern hemisphere (NH, shown in blue and green) and in the Southern hemispheres (SH, shown in orange and red) during high (HSA, shown in blue and orange) and low solar activity (LSA, shown in green and red) in different regions: (a) equatorial (low) latitudes; (b) mid-latitudes; (c) high latitudes (auroral oval); (d) polar caps. The lowest and highest points on the box-plot (i.e., the boundary of the lower and upper whisker) are the minimum and maximum values of the data set (excluding any outliers). The box is drawn from lower (25%) to upper (75%) quartile percentiles with a horizontal line to denote the median value. The Y-axis shows the number of measurements of density. To keep the clarity in this semi-logarithmic plot, we start plotting the Y-axis from the number of counts greater than 100. The top panels correspond to the distributions in the NH while the bottom panels to the SH; left panels are for the high solar activity (HSA), and right panels are for the low solar activity (LSA). We can see that the values of the electron density at equatorial latitudes significantly prevail over other regions.
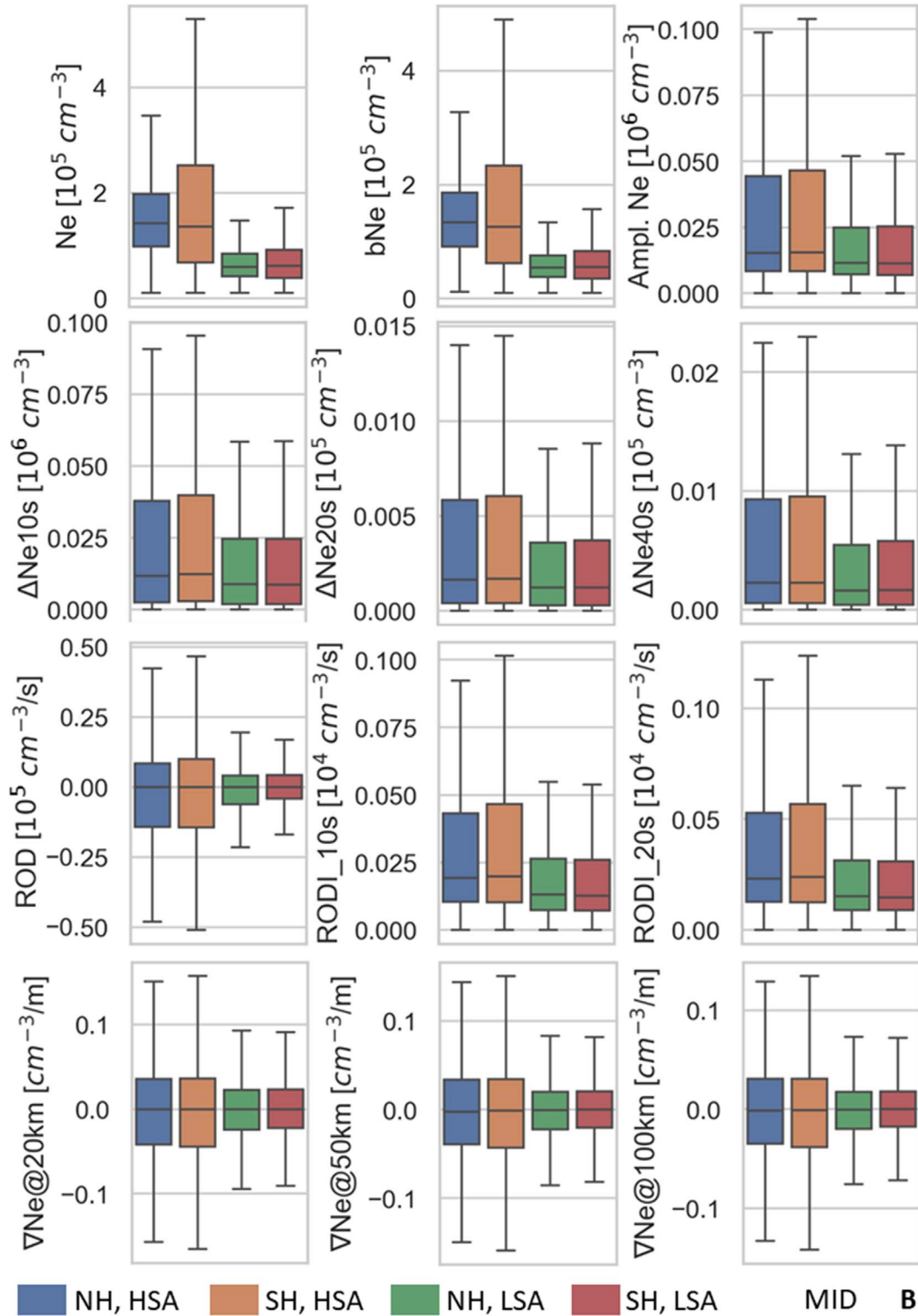
Fig. 1. Continued.

2510 cm^{-3} and 860 cm^{-3} for HSA and LSA, for the SH – 2870 cm^{-3} and 1120 cm^{-3}, respectively).

It can be concluded that during the period of LSA, there is a significant impact on the plasma variability due to large ionospheric structures in the high-latitude region: the high-latitude trough (Jones et al., 1990) and the auroral oval. This is clear in the plots for the SH, where this region is characterized by higher values of RODI than the polar cap.
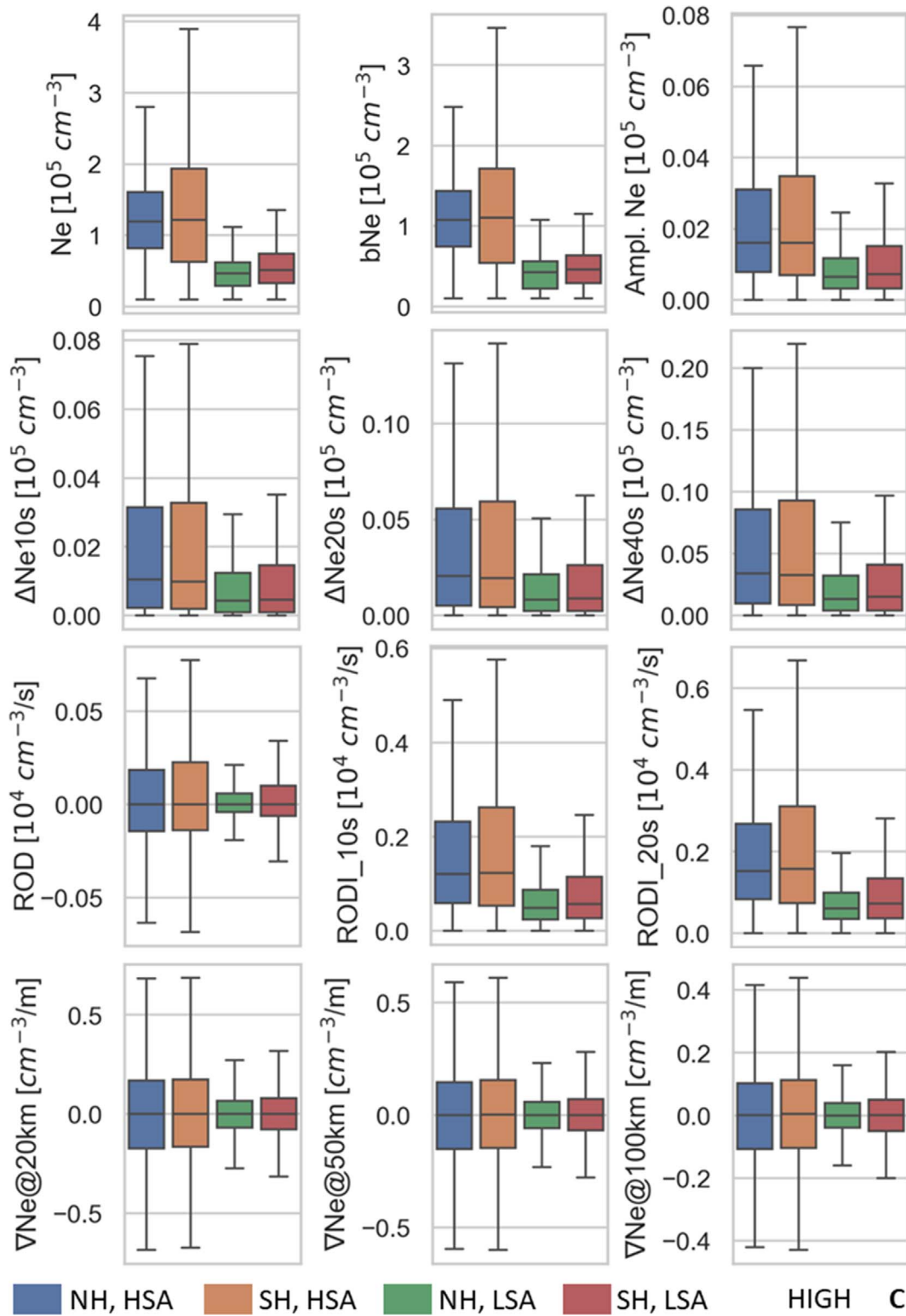
Fig. 1. Continued.

The low latitude region shows similar distributions during HSA for both hemispheres, while during LSA, there are higher maximum values of RODI observed in the NH as compared to the SH. Other regions during HSA show different distributions with higher values in the SH, as shown in Figures 1b–1d. During LSA in the NH, the three regions of mid-, auroral oval, and polar cap latitudes show approximately the same distributions and values of RODI.
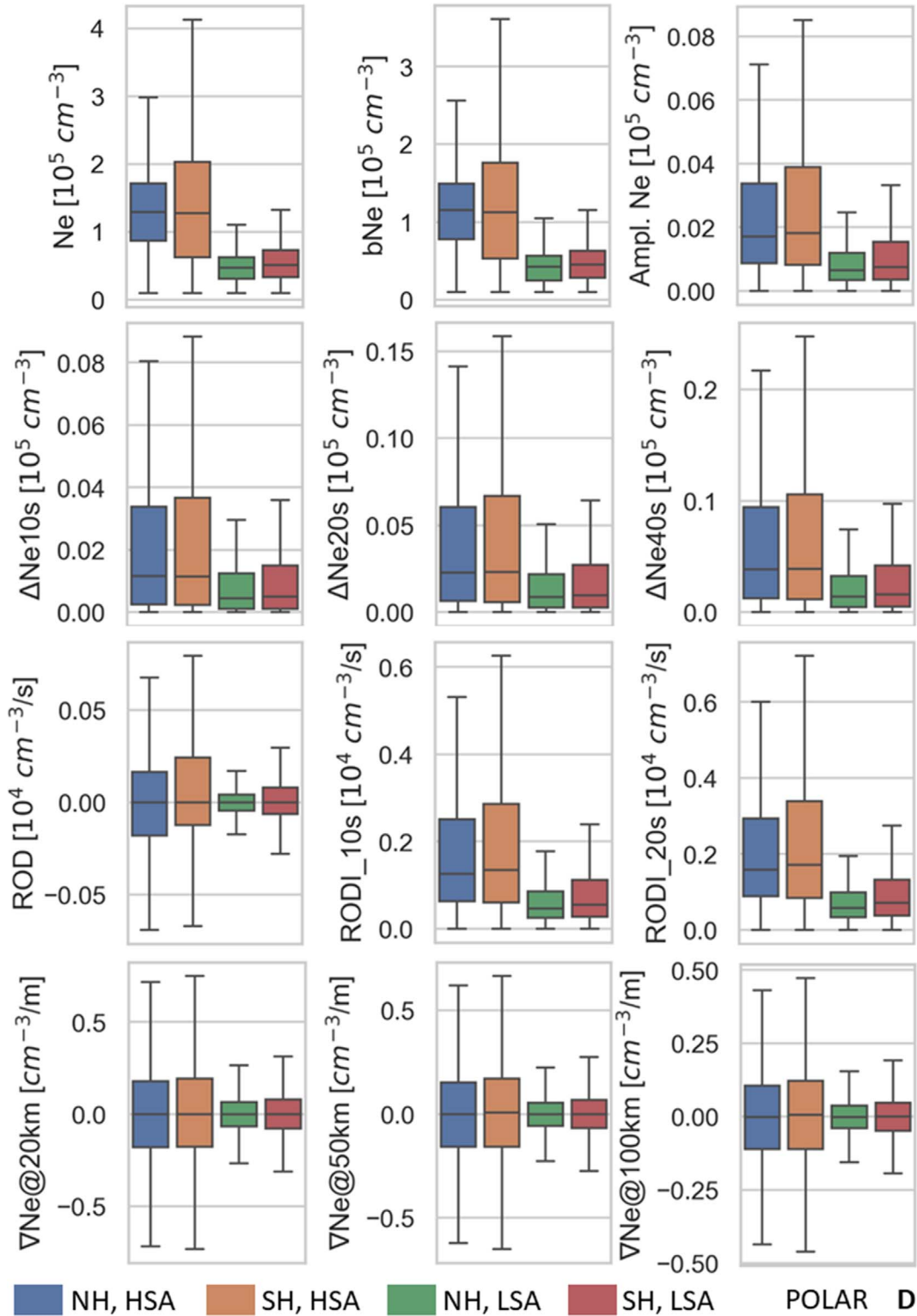
Fig. 1. Continued.

These results are in a good agreement with the results for ROD, and similar distributions were obtained for amplitudes of *Ne* fluctuations, A(*Ne*) (see Supplementary Materials). As before, the minimum values of the parameters are obtained at mid-latitudes. There is a strong correlation between the results for the A(*Ne*) and filtered *Ne* in 10 s (Δ*Ne*) (see Eq. (4)). Similar to RODI and A(*Ne*), Δ*Ne* and gradient of *Ne* at the 20 km scale in the polar cap region reach higher values as compared to
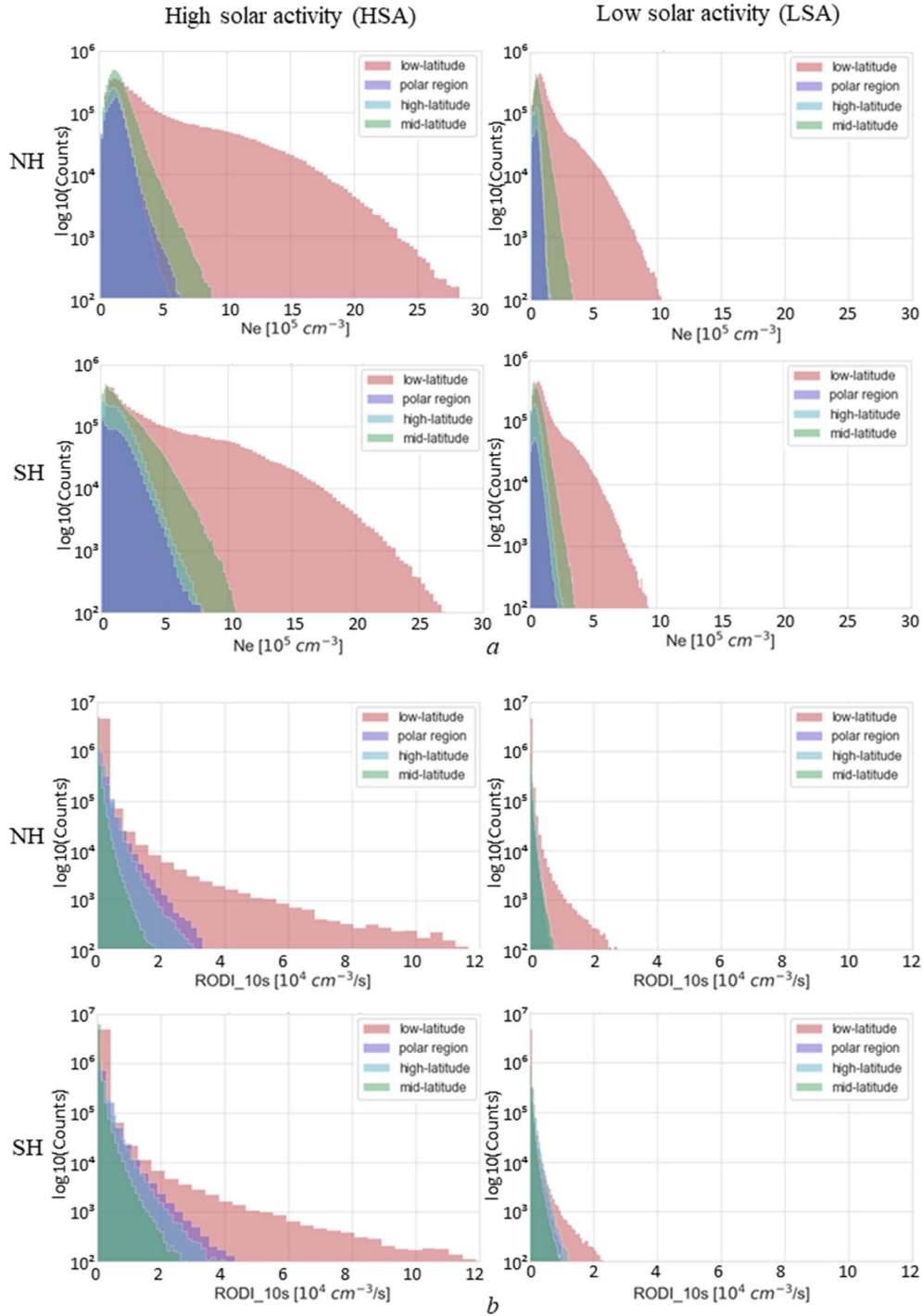
Fig. 2. Distributions of the electron density (*Ne*) (a) and rate of change density index in 10 s (RODI) (b) measured by Swarm A in Northern (top) and Southern (bottom) hemispheres during the year with high (left) and low (right) solar activity levels. The red color shows the distribution in the low latitude region, green in the mid-latitude, blue in the high latitude, and purple in the polar cap regions.

mid- and high-latitudes. However, in the SH during solar minimum, the values of all these parameters are larger at high latitudes compared to the polar cap and are still lower than at low latitudes. This indicates the presence of irregularities of various scales that are captured by the considered parameters. Figures including distributions of these parameters can be found in the Supplementary Materials.

A similar analysis was carried out for Swarm C and Swarm B. Figure 3 shows, as an example, the distribution of the electron density, *Ne*, and RODI across latitudinal regions in the NH as measured by Swarm C and Swarm B during a period of HSA. Swarm A (Fig. 2) and Swarm C (Fig. 3 left) form the lower pair of satellites with separation by 1.4° in longitude. Since the satellites fly close to each other, the results based on
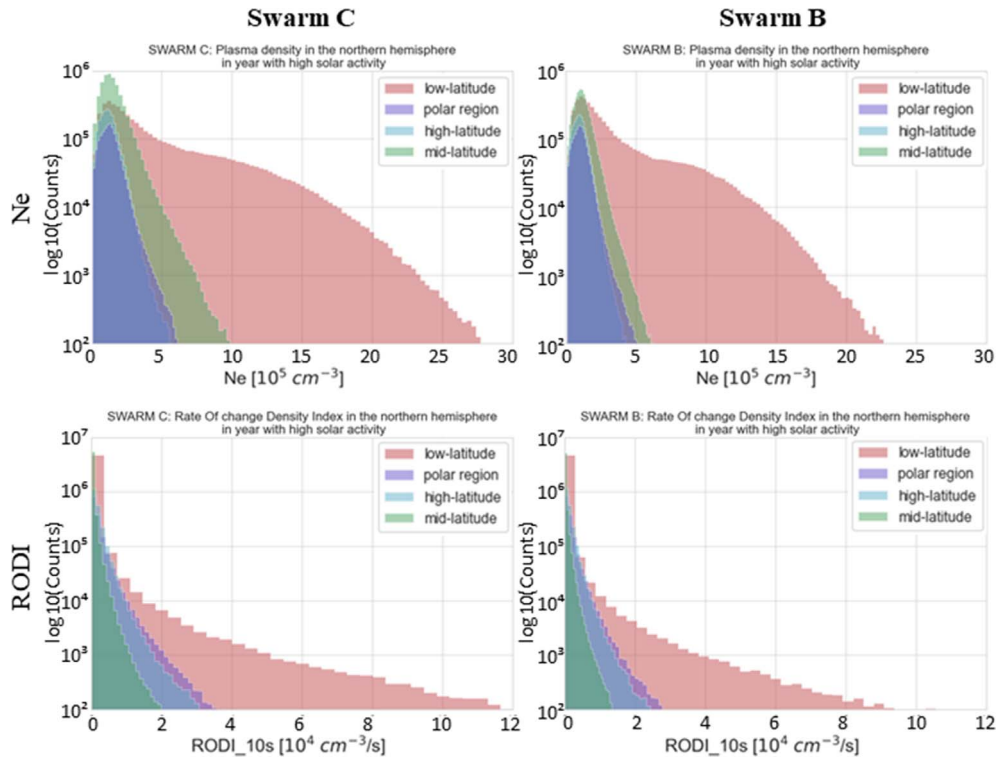
Fig. 3. Distribution of electron density, *Ne*, (top) and RODI (bottom) measured by Swarm C (left) and Swarm B (right) in the Northern hemisphere during high solar activity. The red color shows the distribution in the low latitude region, green in the mid-latitude, blue in the high latitude (auroral oval), and purple in the polar cap regions.

data from Swarm C are similar to those from Swarm A. It is worth noting that over time there is a change in the mission con-stellation associated with the evolution of the orbits (https://earth.esa.int/eogateway/eogateway/missions/swarm/constellation-and-orbit-evolution). When comparing with Figure 2, we see that the general characteristics of distributions at different latitudinal regions are preserved: (1) There is more plasma den-sity produced in the low- and mid-latitude regions (due to solar radiation); (2) There is higher plasma variability observed in the low-latitude region and high structuring observed at higher latitudes. This is also valid for other parameters considered in this study (not shown in Fig. 3). Despite the fact that the flight altitudes of the considered satellites differ by approximately 80 km, the statistics from Swarm B show lower maximal val-ues, which is also related to the electron density profile in the ionosphere, which decreases with increasing altitude. Note that the *Ne* values at low and mid-latitudes, which are based on Swarm B, are significantly lower (by up to 40%) than the values corresponding to Swarm C (see left and right columns in Fig. 3). While at high latitudes and in the polar cap, we see approximately the same values for both satellites.

The differences between Swarm B and the lower pair of the Swarm satellites at low latitudes can be related to the geometry of the magnetic field and related plasma structuring. At high latitudes, the plasma structures are stretched vertically due to the magnetic field lines geometry thus, it is expected that distri-butions obtained by analyzing data from all satellites will be similar. The active nature of the low-latitude ionosphere (e.g., equatorial anomaly, plasma fountain, equatorial electrojet, and plasma bubbles) is due to the horizontal orientation of the

geomagnetic field at the geomagnetic equator (Balan et al., 1997). At equatorial latitudes, the fountain effect and equatorial anomaly are due to the vertical upward drift of plasma across the geomagnetic field lines due to $\mathbf{E} \times \mathbf{B}$ forces and under the influence of gravity and pressure gradient forces the subse-quent downward diffusion of plasma along the geomagnetic field lines to higher latitudes (Hanson & Moffett, 1966). Thus, the actual distributions in electron density at low- and mid-latitudes may significantly differ with the altitude. In all regions, the maximal values of RODI from Swarm B show lower values as compared to Swarm C, which is again consistent with the ionospheric density profile and scale height.

3.2 Distributions fit for Ne and RODI

To apply our results to modeling or predicting ionospheric parameters in different regions, we also found distribution fits for *Ne* and RODI from Swarm A based on a sum of squares error. When evaluating fits for RODI distributions, we did not take into account the values on the right tail of the distribution because their number is insignificant. Whereas the distribution of *Ne* values looks more concentrated, with a low spread of values. We used a list of selected probability density functions (PDFs): normal, lognormal, gamma, log-gamma, exponential, exponentially modified normal, exponentiated Weibull, expo-nential power, Student's *t*, and chi-continuous random variable. For each PDF, we checked the sum of square error between the distribution's histogram and the data's histogram and deter-mined the best PDF with the least error for each region in both hemispheres with high and low solar activity. The resulting best

Table 1. Fit parameters of Ne and RODI distribution.

		HSA		LSA	
		Ne	RODI	Ne	RODI
Low-latitudes	NH	Lognorm ($s = 0.97$, loc $= 0.08$, scale $= 3.15$)	Lognorm ($s = 0.91$, loc $= -0.00$, scale $= 0.03$)	Exponweib ($a = 11.62$, $c = 0.47$, loc $= 0.03$, scale $= 0.11$)	Exponweib ($a = 65.75$, $c = 0.32$, loc $= -0.00$, scale $= 0.00$)
	SH	Lognorm ($s = 1.10$, loc $= 0.07$, scale $= 2.85$)	Lognorm ($s = 0.94$, loc $= -0.00$, scale $= 0.03$)	Lognorm ($s = 0.81$, loc $= 0.01$, scale $= 1.06$)	Exponweib (a $= 74.71$, $c = 0.31$, loc $= -0.00$, scale $= 0.00$)
Mid-latitudes	NH	Exponweib ($a = 24.07$, $c = 0.83$, loc $= -0.56$, scale $= 0.43$)	Exponweib ($a = 54.14$, $c = 0.27$, loc $= -0.00$, scale $= 0.00$)	Exponnorm ($K = 2.37$, loc $= 0.32$, scale $= 0.15$)	Exponweib ($a = 61.28$, $c = 0.30$, loc $= -0.00$, scale $= 0.00$)
	SH	Gamma ($a = 1.23$, loc $= 0.1$, scale $= 1.37$)	Exponweib ($a = 59.66$, $c = 0.25$, loc $= -0.00$, scale $= 0.00$)	Exponweib ($a = 1.29$, $c = 1.28$, loc $= 0.1$, scale $= 0.57$)	Exponweib ($a = 74.97$, $c = 0.28$, loc $= -0.00$, scale $= 0.00$)
High-latitudes	NH	Chi ($df = 2.0$, loc $= 0.1$, scale $= 0.93$)	Exponweib ($a = 3.17$, $c = 0.63$, loc $= -0.00$, scale $= 0.06$)	Exponweib ($a = 0.39$, $c = 3.06$, loc $= 0.1$, scale $= 0.6$)	Exponweib ($a = 8.78$, $c = 0.52$, loc $= -0.01$, scale $= 0.01$)
	SH	Chi ($df = 1.01$, loc $= 0.1$, scale $= 1.62$)	Exponweib ($a = 2.36$, $c = 0.63$, loc $= -0.00$, scale $= 0.08$)	Chi ($df = 1.24$, loc $= 0.1$, scale $= 0.51$)	Exponweib ($a = 2.31$, $c = 0.68$, loc $= -0.00$, scale $= 0.04$)
Polar caps	NH	T ($df = 5.86$, loc $= 1.30$, scale $= 0.56$)	Lognorm ($s = 0.94$, loc $= -0.01$, scale $= 0.14$)	Exponweib ($a = 0.43$, $c = 2.96$, loc $= 0.1$, scale $= 0.6$)	Lognorm ($s = 0.80$, loc $= -0.01$, scale $= 0.05$)
	SH	Chi ($df = 0.98$, loc $= 0.1$, scale $= 1.73$)	Exponweib ($a = 3.52$, $c = 0.55$, loc $= -0.00$, scale $= 0.05$)	Chi ($df = 1.26$, loc $= 0.1$, scale $= 0.49$)	Lognorm ($s = 0.94$, loc $= -0.00$, scale $= 0.06$)

Here the location (loc) keyword specifies the mean and scale – the standard deviation. For Gamma takes a as a shape parameter.

fits are presented in Table 1, along with the fit parameters. Some examples with good and bad PDFs characterized by these parameters are shown in Figure 4, with the red line overlaying the histogram.

As it can be seen from Table 1, the most common types of PDFs are exponentiated Weibull (in 16 out of 32 cases), lognormal (8/32), and chi (5/32). For the exponentiated Weibull, the PDF is defined as:

$$f(x, a, c) = ac[1 - \exp(-x^c)]^{a-1} \exp(-x^c)x^{c-1} \quad (6)$$

and its cumulative distribution function is:

$$F(x, a, c) = [1 - \exp(-x^c)]^a$$

where $x > 0$, a is the exponentiation parameter, and $a > 0$, c is the shape parameter of the non-exponentiated Weibull law, and $c > 0$.

The PDF for lognormal is:

$$f(x, s) = \frac{1}{sx\sqrt{2\pi}} \exp\left(-\frac{\log^2(x)}{2s^2}\right) \quad (7)$$

where $x > 0$, s is a shape parameter, and $s > 0$.

The PDF for chi is:

$$f(x, k) = \frac{1}{2^{k/2-1}\Gamma(k/2)} x^{k-1} \exp\left(-x^2/2\right) \quad (8)$$

where $x \geq 0$ and $k > 0$ (k degrees of freedom, used as df in Table 1). Γ is the gamma function. The probability density above is defined in the "standardized" form. To shift and/or scale the distributions, we used the *loc* and *scale* parameters as $y = (x - loc)/scale$.

As noted by Pal et al. (2006), the family of the exponentiated exponential distribution is close to the Weibull or gamma family. The Weibull distribution is used to model the wind speed distribution for wind energy analysis (Seguro & Lambert, 2000) and is a generalized gamma distribution. Also, Weibull, lognormal, and gamma densities are similar in shape for the same coefficient of variation (Silva & Lisboa, 2007). Thus, the distribution of the considered ionospheric parameters can be described by closely related families of distribution functions. Therefore, the statistics given in Figure 1 can also be used when analyzing the constructed models or predicting the values of the plasma density parameters of the ionosphere.

The literature on this topic is, in general, very sparse (especially in the context of global studies of the ionosphere), which again shows the importance of the results presented here. The interplanetary magnetic field strength has a distribution that is lognormal to a good approximation (Burlaga & King, 1979). Burlaga & Lazarus (2000) showed that the distribution of the solar wind data (in the hour averages of the density, speed, and proton temperature at 1 astronomical unit) obeys a lognormal PDF. The same result of the lognormal distribution was obtained when Tindale & Chapman (2017) analyzed data of the solar wind plasma parameters from the Wind spacecraft for solar cycles 23 and 24. They notice that the lognormal most closely describes the slow and fast wind data at solar minimum. At solar maximum, particularly in the fast wind, the distribution is less well described by the lognormal model.

Initially, it was assumed that the distribution of ionospheric observations proceeds according to the normal distribution characterized by a mean, standard deviation, median, and quartiles (as an example, see Araujo-Pradere et al., 2003; Bilitza, 2004). However, as noted in Garner et al. (2005), with the normal distribution always exists a nonzero probability of observing any value, including negative values, which are unphysical for the measured ionospheric parameters like electron density or temperature (measured in Kelvins). Garner et al. (2005) in a study based on 10 years of DMSP data for the selected ionospheric area (15.5°–16.5° MLAT), identified lognormal PDF for ionospheric density measurements. It should be noted that outliers were not included. The authors used two cutoff densities: the lower cutoff $\Phi(n_{low}) = 1/N$ and an upper cutoff $\Phi(n_{up}) = 1 - 1/N$, where N is the number of points within the data bin. Any density less than this n_{low} or greater than n_{up} is rejected as an outlier. In addition, Turel & Arikan (2010) examined during 6 years of the GPS-TEC from 18 receivers in different latitudinal regions and showed that they are generally subject to a lognormal distribution. The Weibull distribution also proved to be the best PDF in several studied cases.
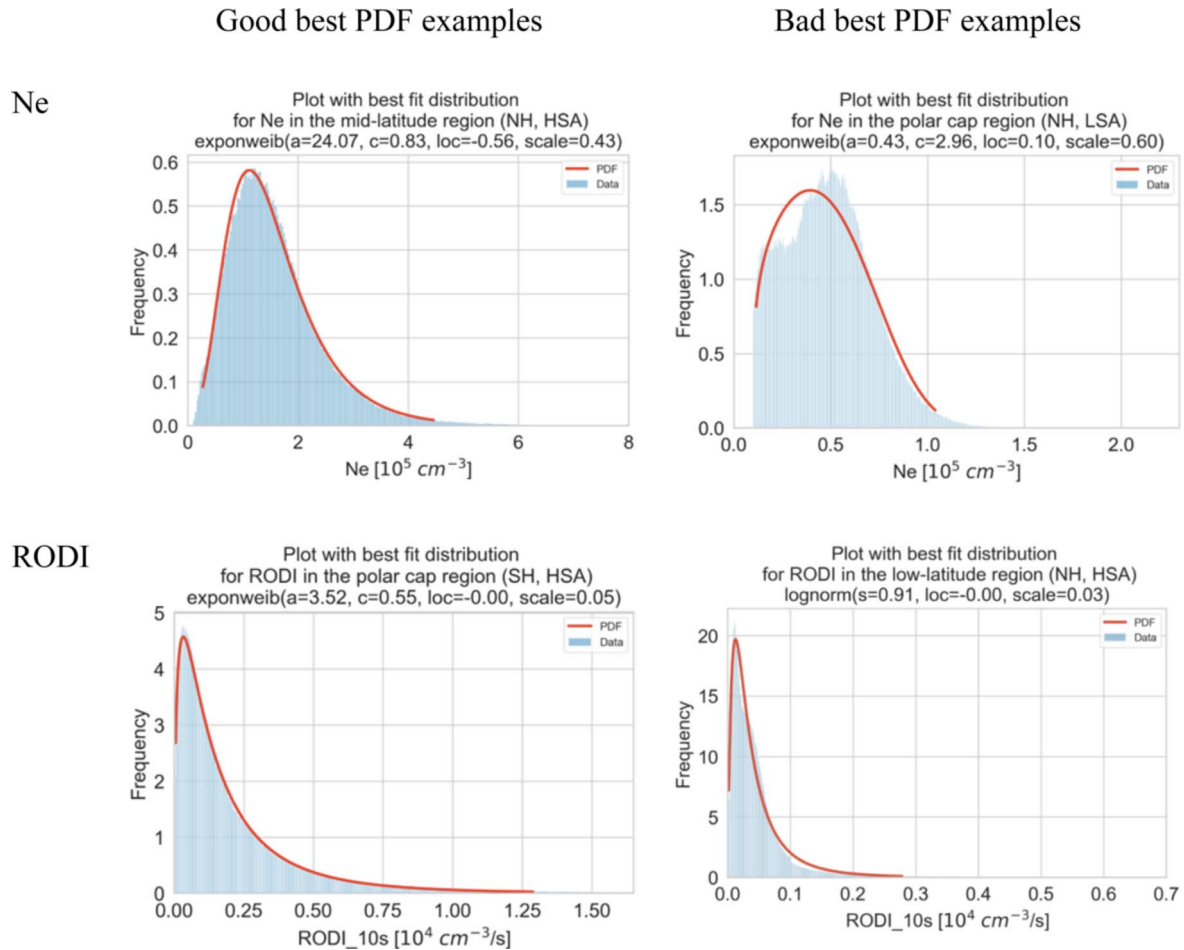
Fig. 4. Examples with a good and bad PDF (red line) of the *Ne* (top) and RODI (bottom) distributions are presented with a blue histogram. All other plots can be found in SM2.

They mentioned that generally, the Weibull distribution is very similar to the lognormal distributions and that the vertical total electron content (VTEC) from the stations located in very high latitudes cannot be described using only one PDF distribution. In our results, the double-peaked features of the electron density distribution at high and low latitudes and the polar cap also are not fully reproduced with selected PDF (all plots with best-fitting PDF for *Ne* and RODI presented in the SM2 and SM3). The opposite result is observed for RODI, when the best fitting PDF is obtained for the polar caps, then for high latitudes, and the worst for low- and mid-latitudes.

3.3 Diurnal variations of *Ne* and RODI

To analyze in detail the distributions presented in the previous section, we now separately consider each geomagnetic region and study diurnal variations to assess the contributions of certain processes.

3.3.1 Low-latitudes

Figure 5 presents the diurnal variation in the electron density (Fig. 5a) and RODI in 10 s (Fig. 5b) at low (equatorial) latitudes for both hemispheres and different solar activity levels.

The range of the *Y*-axis is set as the range of *X*-axis in Figure 2. We used a color bar lower limit of 10 counts to exclude sporadic events. Both hemispheres show similar distributions, with a difference observed near midnight, where the values are higher in the NH, and in the morning hours, where the values are higher in the SH. For LSA, the peak in the *Ne* distribution around 20 MLT, which was observed for HSA, is not present anymore, and instead, the midday maximum is pronounced. The distribution of the number of measurements is uniform across MLT (this is shown as the additional top bar in each of the plots). However, there are small notches corresponding to the dips and rises in the electron density values, which are most likely associated with the post-processing of the dataset and the exclusion of erroneous values. The most commonly observed values (see Fig. 1a) are ~7.2 × 10^5 cm^{-3} and ~1.8 × 10^5 cm^{-3} for HSA and LSA, respectively. It should be noted that the behavior of background density is the same as that of *Ne*.

Figure 5b presents, in the same format, the results for RODI in 10 s. The area with an increase in the amplitude of RODI is clearly visible starting from 19:30 MLT and extending until 04 MLT in the morning. This prolonged maximum is associated with the equatorial plasma bubbles, and our results concur with the work of Smith & Heelis (2017), where the indicated

altitudes of the plasma bubbles also correspond to the altitudes of the Swarm satellites. In general, the obtained diurnal variation of both considered parameters is very symmetric between the hemispheres, which reflects the mechanisms behind the equatorial anomaly. Strong plasma irregularities located near the magnetic equator and lasting from dusk to early morning correspond to one of the three main regions where the ionospheric irregularities are present (Jin et al., 2020).

Data shown in Figures 5 and 6 are after filtering described in Section 2. It should be noted that the box-plots with whiskers (Fig. 1) and distributions (Fig. 2) do not change much after filtering. However, the filtering leads to the appearance of localized minima in the RODI plots (see Figs. 5b and 6b) during selected time intervals.

3.3.2 Mid-latitudes

Figure 6 shows the results of the diurnal variation of the electron density Ne and RODI for the mid-latitude region. The mid-latitudes are a transitional region between the equatorial to the high-latitude ionosphere, and thus one would expect to observe similar patterns for the NH and SH as at low latitudes. However, during HSA, we see a clear hemispheric asymmetry with higher Ne values in the SH. In fact, this pattern also persists when considering the full distribution over 7 years. The general result is an increase in the electron density in the morning hours and at nighttime in the SH. The midday increase in electron density can easily be noted, which connects with low solar zenith angle and high ionization rate. The second increase, which is not so significant but still present, can be observed in the time period between 20 and 06 UT, and it is more visible in figures for LSA.

Aa et al.'s (2020) statistical article on the topside main ionospheric trough describes its key features such as the occurrence rate, position, depth and width. The article is also based on in situ plasma density measurements from Swarm. The authors show that for both hemispheres, the time with the highest occurrence and lower MLAT position of the main ionospheric trough (about 55°–65° MLAT) coincides with the time interval that we have identified (from the evening until the morning). The mid-latitude region may contain the contribution of the main ionospheric trough since its northern boundary of the region is determined by the position of the auroral oval. The daily variation of Ne during LSA is approximately the same for both hemispheres (with a larger value in the SH). We see a small pre-noon increase (from 10 to 12 MLT) in the Ne for the SH. The corresponding peak is visible during HSA. The distribution of the background density is the same as that for Ne.

To understand the increase of Ne at night and during morning hours in the SH, we plot the distribution of Ne versus geomagnetic latitude and longitude for the selected time interval 00–06 MLT (see Supplementary Materials Fig. SM4). The largest Ne values correspond to the region centered at −55° MLAT and within the interval of magnetic longitude from −40° to 60°. This position and observation time correspond to the Weddell Sea anomalies, which can also be observed at the height of the Swarm passes (Lin et al., 2009; Karpachev et al., 2011).

The distribution of RODI in the SH shows higher values than in the NH, in particular during HSA (see Fig. 1b). The sharp decrease in the electron density in the early morning leads to the increased RODI values around 04 MLT (which is especially clear during LSA). It can be noted that this peak in RODI is observed somewhat earlier in the NH (before 04 MLT) than for SH (after 04 MLT). The presence of this disturbance in RODI, as well as a significant decrease in Ne, can again be associated with the main ionospheric trough. Indeed, as Aa et al. (2020) observe, the statistical position of the trough minimum is around 04 MLT. After this, a rapid displacement of the trough toward the pole up to 15° is usually observed, as well as a decrease in the trough occurrence rate (down to its disappearance).

3.3.3 High-latitudes (auroral oval)

The results for Ne and RODI at high latitudes are presented in Figure 7. The maximum values of RODI in this region are almost twice the maximum for mid-latitudes, while the electron density values are generally lower. This indicates a high variability of the high-latitude region. Since this region is clearly marked in the IPIR data product by the position of the auroral oval, the influence of the main ionospheric trough, which existed for the previous region, is diminished here. There is a clearly observed peak in Ne around 12–13 MLT, as well as its manifestation in RODI during HSA. In the SH, both variables can reach higher values. For example, the average maximum diurnal value of Ne in the SH during HSA is about 4×10^5 cm^{-3} while for the NH is 3×10^5 cm^{-3} (see Fig. 7a). The diurnal variations Ne in the NH are clear, with higher average density in the afternoon sector, and show less scatter than in the SH. The small increases in RODI at night can be related to auroral processes. This was also shown earlier that irregularities are mostly observed in the dayside cusp, polar caps, and nightside auroral oval (Jin et al., 2019).

3.3.4 Polar caps

The distributions of Ne and RODI as a function of MLT in the polar caps are shown in Figure 8. This analysis used an upper threshold of ±81° MLAT to facilitate a temporal separation due to converging MLT towards magnetic poles. Thus, data above ±81° MLAT was not used in this analysis.

The results for LSA show a similar pattern as the distribution obtained in the period of HSA. The presence of reduced statistics around noon in the electron density in both hemispheres is interesting (with the number of counts shown with color). It can be explained by the statistics of satellite orbits: in the period near noon, the total number of passes is lower in comparison with nighttime (see the upper histograms in the figures). It should be noted that, despite the same number of measurements, this depletion is not observed in the RODI data. This feature in the Ne distribution is more pronounced during LSA, and it is clearly seen in the background Ne plots (see Supplementary Materials Fig. SM5). The electron density reached extremely low values during all MLT with the year of LSA (see Fig. 1d, where the median Ne reaches 4.76×10^4 cm^{-3} in the NH and 5.12×10^4 cm^{-3} in the SH). However, at nighttime, between 21–06 MLT at 70°–80° MLAT during the solar minimum in the winter polar ionosphere, the electron density can reach even much lower values down to about 2×10^2 cm^{-3} (Crowley et al., 1993). It is clearly seen that the diurnal variation is different for the NH and SH. The largest asymmetry between both hemispheres in the
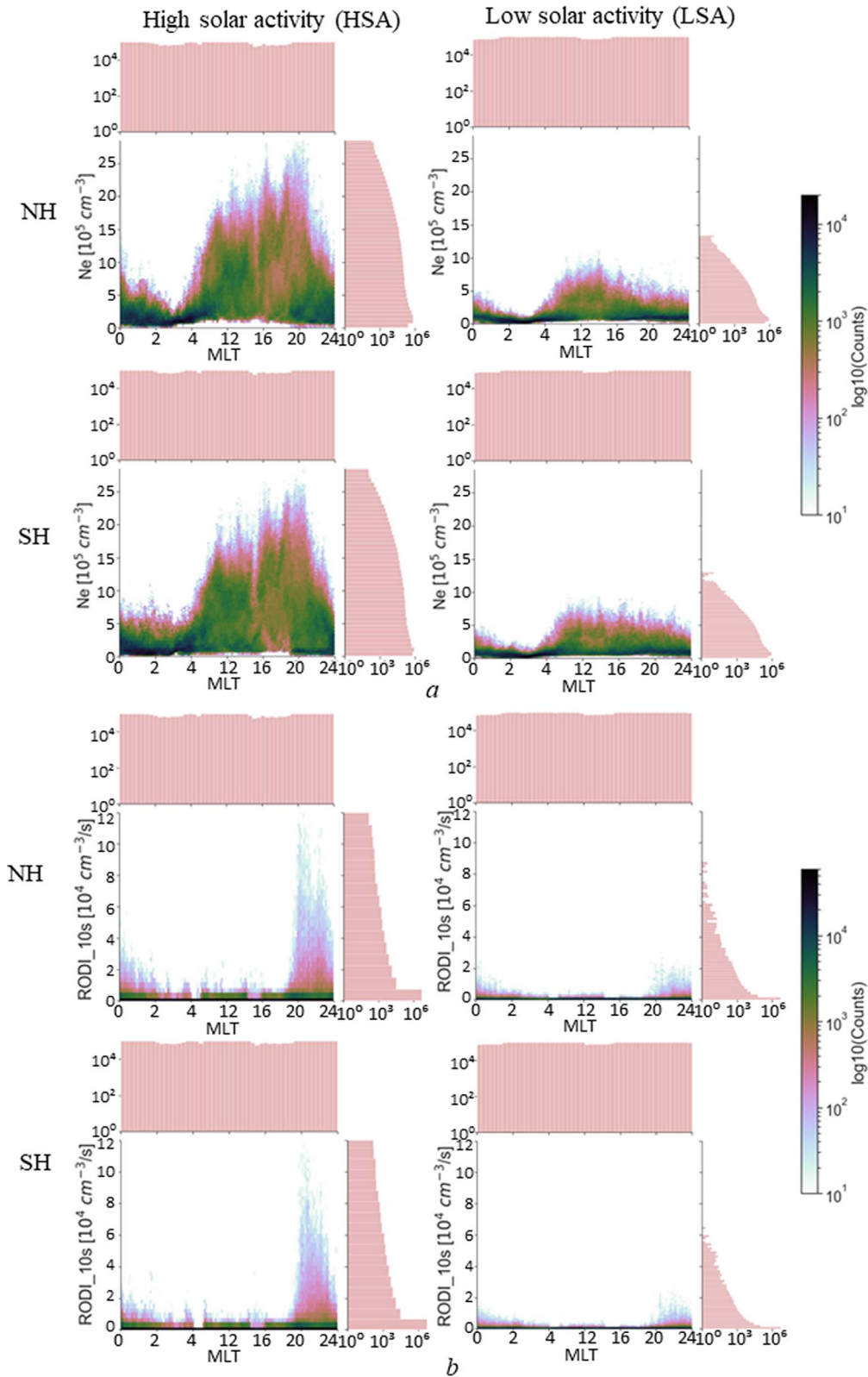
Fig. 5. The diurnal variations of the electron density *Ne* (a) and the rate of change density index in 10 s (RODI) (b) in the equatorial region for the NH (top) and SH (bottom) during HSA (left) and LSA (right). Additional bars to the right present the cumulative distribution of the results at a given value. The bars above the distribution show the statistics of the measurements at a given MLT. The color bar shows the density of counts, and it is the same scale for all plots. The *Y*-axis limit corresponds to the *X*-axis limits of each region in Figure 2.
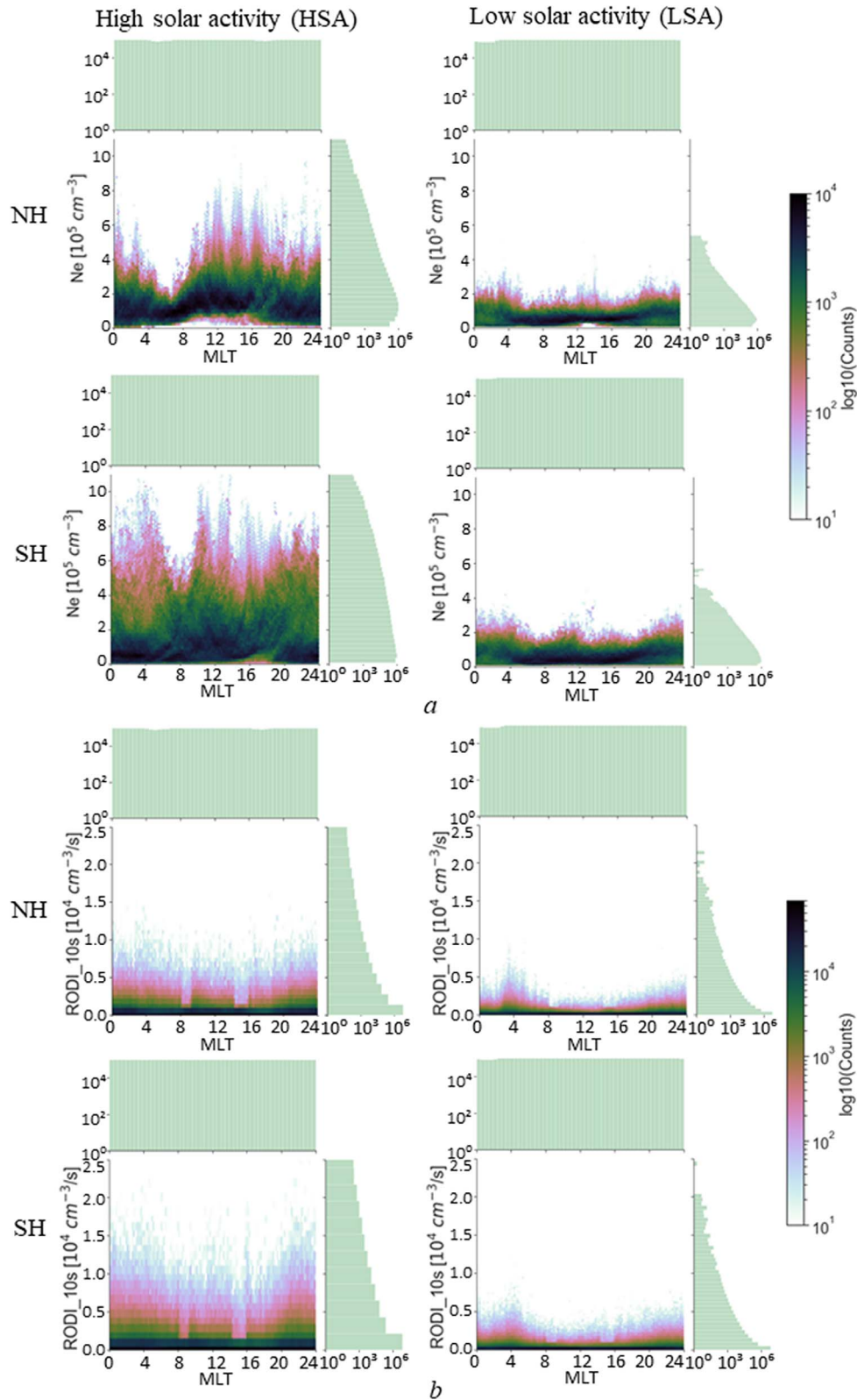
Fig. 6. Same as Figure 5 but for the mid-latitude region.

Ne distribution is observed in the polar caps. Despite the fact that the satellite's altitude over the southern polar cap is on average 10–15 km higher than over the northern one, in general, large values of both the maximum *Ne* and RODI were obtained in the SH. This can be related to the asymmetry in the Earth's magnetic field and different offset between the magnetic and geographic poles (7° in the NH vs. 16° in the SH) (Laundal et al., 2017).
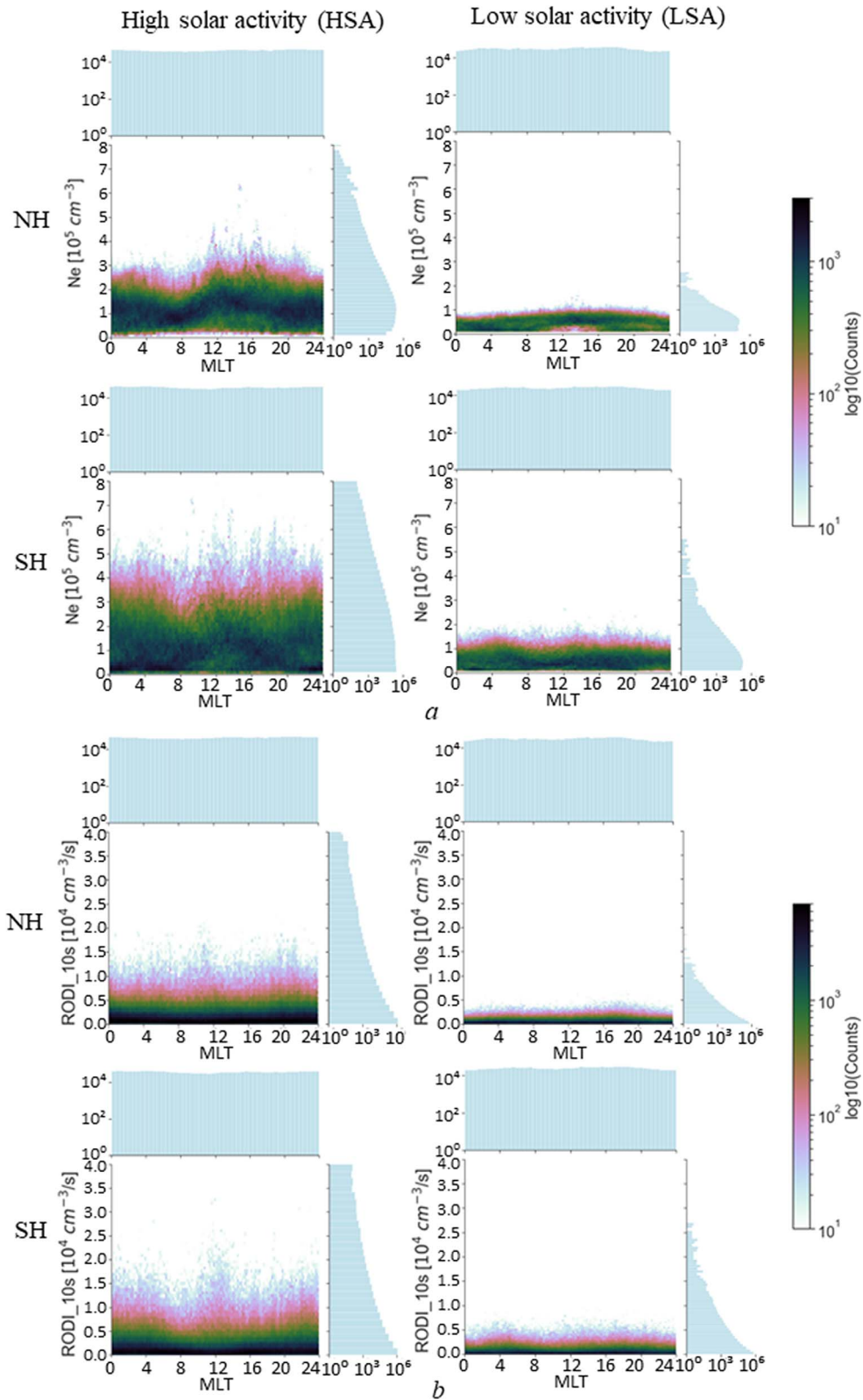
Fig. 7. Same as Figure 5 but for the high-latitude region (auroral oval).

In addition, a 50% decrease in *Ne* was observed in the NH during HSA in the early morning sector (04–07 MLT). This concurred with the results obtained by Bjoland et al. (2021) with the incoherent scatter EISCAT Svalbard Radar (ESR) located at 75.43° N geomagnetic latitude. Based on several decades of measurements, they found that one of the reasons for the
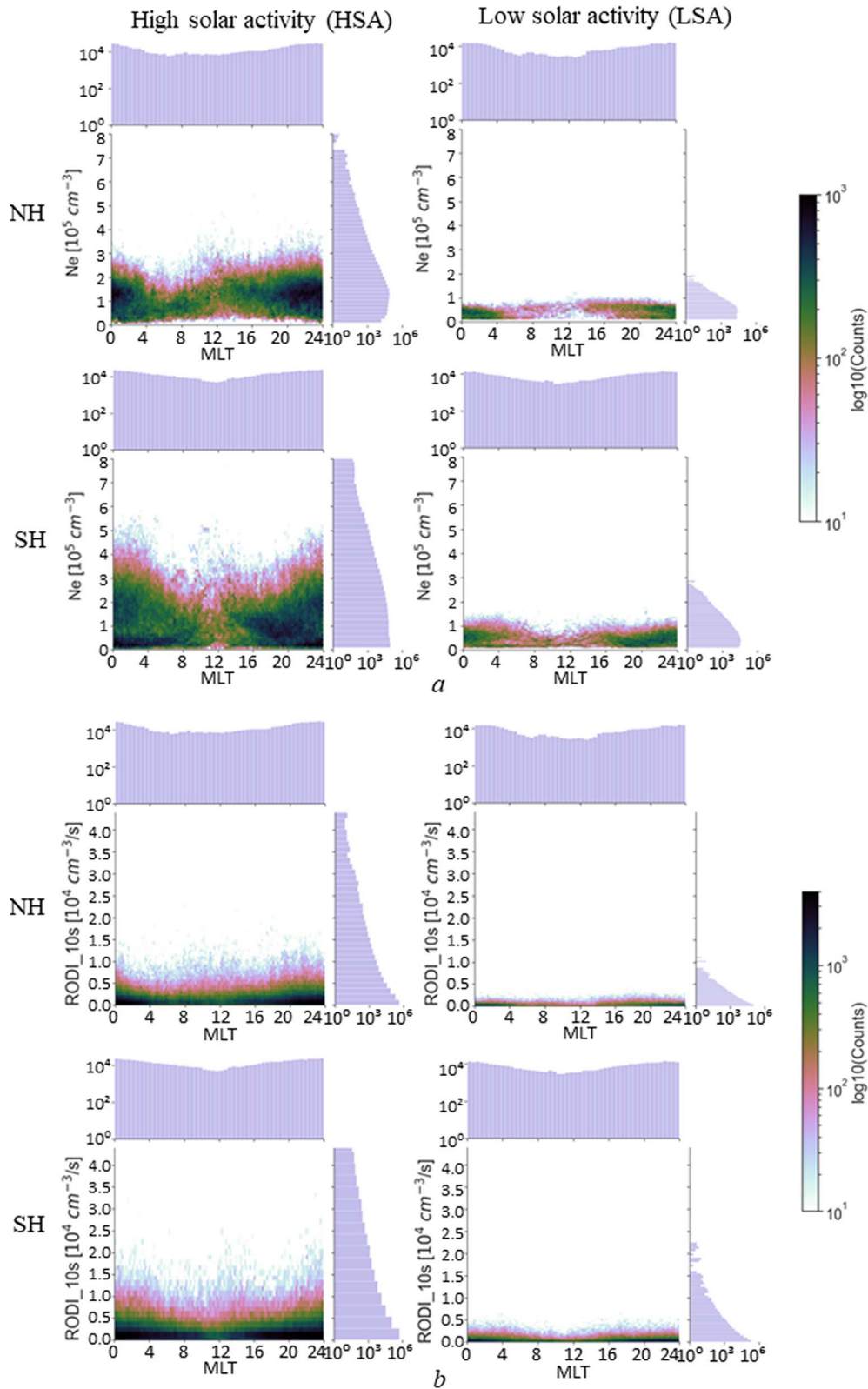
Fig. 8. Same as Figure 5 but for polar region (polar caps).

electron density depletion is an enhancement in the ion temperature in this region. It can be noted that such a depletion of *Ne* has not yet been observed in the SH, which may be a separate topic for future research. We assume (since seasonal changes in the solar zenith angle could also contribute to the formation of the depletion region, Bjoland et al., 2021) that the difference in

changes in the zenith angle of the Sun in both hemispheres (discussed in Laundal et al., 2017) may be the cause of this asymmetry.

One of the main sources for scintillations of the satellite signals in the polar cap region are the polar cap patches (PCP). The mechanism of PCP's formation and occurrence have been studied in detail and presented in previous work (Spicher et al., 2017; Chartier et al., 2018; Jin & Xiong, 2020; Kagawa et al., 2020). It is known that a distinctive feature of PCP is that the plasma density value in the F region is at least doubled in comparison with the background value (Crowley, 1996). It should be noted that although a remarkable feature of the Swarm satellites is their coverage of the polar regions, the altitude of the satellites' flight is higher than the altitude of the location of the maxima in the electron density as a peak patch density (see Rodger et al., 1994; Lorentzen et al., 2004). However, due to the frozen-in condition, it is possible to assess the distribution of these structures based on the measurement data at the Swarm altitudes.

We can draw the following conclusions regarding our results. In general, the values at night prevail over the day (especially during HSA). Heppner & Maynard (1987) show that depending on the orientation of the IMF B_y component and followed polar convection model, the larger number of PCPs observed on the dawnside and duskside. While we do not present a separation according to the IMF B_y, we can note, on the whole, increased RODI values at this time of the day. We see a local enhancement in the Ne around noon in the SH with the same amplitude as at night time, leading to an increase of RODI. Based on previous results (Rodger & Graham, 1996; Noja et al., 2013; Spicher et al., 2017), we can associate this peak with structuring within PCPs. These authors also marked that in the SH, the maximum of PCPs' occurrence is centered around magnetic noon. Coley & Heelis (1998) and Noja et al. (2013) found at least twice more patches in the SH as in the NH. This also can be related to higher values of RODI in the SH compared to the NH. However, it is worth noting that Noja et al. (2013) used the PCP detection technique (using CHAMP TEC data) that relies on determining a positive slope in the TEC data followed by a negative slope in a sliding window. They do not put restrictions on the spatial size of the slope and use a mixture of absolute and relative patch magnitudes as a detection approach. Thus, Ne sharp peaks can also be identified as PCP. Their analysis includes data from 55° MLAT, which may contain auroral phenomena. Therefore, their statistics may also include other phenomena.

4 Summary and conclusion

For the first time, we present a global statistical study, which also contains information on the shape of the distribution and PDF of electron density and derived ionospheric parameters. The distribution of ionospheric parameters is examined for different levels of solar activity, latitudinal regions, magnetic local times, and hemispheres. We considered one year of data with high solar activity and one year of data with low solar activity. The analysis of two years of data for both levels of solar activity is sufficient to cover all local times (keep in mind that in this work, we did not consider seasons separately). We presented an analysis including all days with both high and low geomagnetic activity. It should be noted that the total number of days with

the Kp index above 5 is a small part in the context of the whole-year dataset: 35 (13) days for high (low) solar activity. The study of distributions and statistics of parameters for quiet geomagnetic conditions is outside the scope of the present study and is our ongoing research that will provide a baseline important for other model studies. However, the PCP occurrence does not depend much on the geomagnetic activity expressed in the Kp index (Dandekar & Bullett, 1999).

Our statistical results not only confirmed a number of previously published studies in specified regions but also revealed new features. The new results demonstrated that PDFs for Ne and RODI can be used in the characterization of spatial variability for low-, mid-, high-latitude regions and polar caps. To do this, we checked ten different PDFs on the histograms in order to obtain the best fitting parametric distributions by determining the minimum value of a sum of squares error. We found that, for Ne histograms, the predominant types of PDF are an exponentiated Weibull (in 5 out of 16 cases), a chi (5/16), and a lognormal (2/16). The Ne distribution at low latitudes is more subject to a lognormal distribution, while in the high latitude region, the chi distribution prevails. As noted in the work of Silva & Lisboa (2007), exponentiated Weibull, lognormal, and gamma distributions are very close to each other. Chi distribution is related to the chi-squared distribution, which is also a special case of the gamma distribution. Thus, the prevailing types of PDF are similar. There are also gamma, exponentially modified normal, and Student's t distributions. Distribution types differ for the NH and SH (with predominant exponentiated Weibull in the NH and chi distribution in the SH). It can be noted that the Ne distribution at high latitudes and polar caps is described to a greater extent by the chi PDF. In general, we found that the best fitting is obtained at mid-latitudes, and the worst is obtained for the two-peak structure (especially during the LSA period) at high-latitudes and polar caps.

With regard to the distributions of RODI, completely different results were obtained. There are only two types of distribution with a predominant exponentiated Weibull (11/16 vs. 5/16 as lognormal). Thus, the best distribution for describing the behavior of RODI (especially in mid and high latitudes) is the exponentiated Weibull. The fitted PDFs also look symmetrical for the NH and SH, with a better agreement for high latitudes and polar caps than for low and mid-latitudes. In general, the data histograms can be directly used as experimental PDFs, and they are beneficial in obtaining a parametric PDF. Such statistical characterization of the ionosphere is very important for developing predictive models, machine learning, and testing or improving existing assimilation, deterministic and empirical models of the ionosphere. As mentored in Garner et al. (2005), if ionospheric densities are better characterized by lognormal distributions, then empirical models will need to report more than one value to specify a climate. The information in this study is also useful for the design and development of new satellite missions.

The obtained diurnal variations of the ionospheric parameters are in good agreement with the results of other scientific groups obtained from diverse observational data. We select the following main results:

1. There is a larger variability of ROD, RODI, electron density gradient, and amplitude at low latitudes and in the polar cap compared to mid- and high-latitudes.

2. Comparing both hemispheres during the solar minimum, we obtained higher values of the electron density gradients and amplitudes, ROD and RODI, in the Southern hemisphere at high latitudes and in the polar caps, while for the Northern hemisphere, higher values were obtained at low latitudes.

3. With increasing altitude in the range of the Swarm satellites, the maximum values of the electron density decrease in the region of low and mid-latitudes but do not change for high and polar ones.

4. The main patterns of the diurnal variation of the parameters in different regions do not depend on the level of solar activity (which affects only the maximum values).

5. There is a depletion of Ne in the early morning sector (04–07 MLT) in the polar cap region in the NH. Such a depletion of Ne has not yet been observed in the SH, which may be a separate topic for future research.

This research may have implications for the development of new satellite instruments and the accuracy of GNSS precise positioning. Alternatively, it can be used as an input for climatological models: which scales are dominant, which conditions, or fluctuations. Thus, we show the climatology of plasma variability in the ionosphere.

This study was carried out using an IPIR data product based on in situ plasma density data from the Swarm satellites. The IPIR data product makes it possible to assess the distribution of plasma irregularities of various scales with reference to regions. This separation allows one to reveal the influence of the main processes in each region, such as plasma bubbles, equatorial anomaly, Weddell Sea anomaly, main ionospheric trough, precipitation of auroral particles, and shift of the auroral oval, polar cap patches. This data product can be used by the scientific community for both rapid assessments of the state of the ionospheric plasma (https://vires.services/) and for systematic analysis of the impact of space weather both locally and globally.

Supplementary materials

Supplementary material is available at https://www.swsc-journal.org/10.1051/swsc/2022007/olm

Figure SM0. The hourly averaged solar radio flux F10.7 index in years 2010–2020. The red (blue) shaded area shows the time interval selected as high (low) solar activity level, respectively.

Figure SM1. Variability of background electron density (bNe) (a), Rate Of change Density (ROD) (b), Amplitude of Ne (c), filtered Ne in 10 s (d) and gradient Ne in 20 km scale (e) measured by Swarm A in the Northern (top) and Southern (bottom) hemispheres during the year with high (left) and low (right) solar activity levels. The red color shows the distribution in the low latitude region, green - in the mid-latitude, blue - in the high latitude and purple – in the polar region. Histograms for each parameter are presented on the same scale.

Figure SM2. Plots with the best fit (red line) distribution (blue histogram) for electron density Ne in different regions for the Northern (NH) and Southern (SH) hemispheres during high (left) and low (right) solar activity levels. The name of the PDF is presented with fit parameters.

Figure SM3. Plots with best fit (red line) distribution (blue histogram) for RODI in 10 s in different regions for the Northern (NH) and Southern (SH) hemispheres during high (left) and low (right) solar activity levels. The name of the PDF is presented with fit parameters.

Figure SM4. Distribution of the electron density Ne versus geomagnetic longitude (a) and latitude (b) for the selected time interval from 0 to 6 MLT. Diurnal variation of the Ne in the area MLAT ($-65°$; $-45°$) and MLON ($-40°$; $60°$) shows an effect of the Weddell Sea Anomaly (c) at night and in the morning hours.

Figure SM5. The diurnal variation of the background electron density bNe in the polar cap region for the Northern (top) and Southern (bottom) hemispheres during high (left) and low (right) solar activity levels. Additional plots present distribution with such values on a logarithmic scale. The colour bar shows the density of counts in the same scale for all plots. The Y-axis limit based on Figure SM1.

References

Aa E, Zou S, Erickson PJ, Zhang S-R, Liu S. 2020. Statistical analysis of the main ionospheric trough using swarm in situ measurements. *J Geophys Res* **125(3)**: e2019JA027583. https://doi.org/10.1029/2019JA027583.

Araujo-Pradere EA, Fuller-Rowell TJ, Bilitza D. 2003. Validation of the STORM response in IRI2000. *J Geophys Res* **108(A3)**: 1120. https://doi.org/10.1029/2002JA009720.

Balan N, Bailey GJ, Abdu MA, Oyama KI, Richards PG, et al. 1997. Equatorial plasma fountain and its effects over three locations: Evidence for an additional layer, the F3 layer. *J Geophys Res* **102(A2)**: 2047–2056. https://doi.org/10.1029/95JA02639.

Basu S, MacKenzie E, Basu S. 1988. Ionospheric constraints on VHF/UHF communications links during solar maximum and minimum periods. *Radio Sci* **23(3)**: 363–378. https://doi.org/10.1029/RS023i003p00363.

Basu S, Basu S, MacKenzie E, Coley WR, Sharber JR, et al. 1990. Plasma structuring by the gradient drift instability at high latitudes and comparison with velocity shear driven processes. *J Geophys Res* **95(A6)**: 7799–7818. https://doi.org/10.1029/JA095iA06p07799.

Bilitza D. 2004. A correction for the IRI topside electron density model based on Alouette/ISIS topside sounder data. *Adv Space Res* **33**: 838. https://doi.org/10.1016/j.asr.2003.07.009.

Bilitza D, Reinisch BW. 2008. International reference ionosphere 2007: Improvements and new parameters. *Adv Space Res* **42(4)**: 599–609. https://doi.org/10.1016/j.asr.2007.07.048.

Bjoland LM, Ogawa Y, Løvhaug UP, Lorentzen DA, Hatch SM, et al. 2021. Electron density depletion region observed in the polar cap ionosphere. *J Geophys Res* **126(1)**: e2020JA028432. https://doi.org/10.1029/2020JA028432.

Burlaga LF, King JH. 1979. Intense interplanetary magnetic fields observed by geocentric spacecraft during 1963–1975. *J Geophys Res* **84**: 6633. https://doi.org/10.1029/JA084iA11p06633.

Burlaga LF, Lazarus A. 2000. Lognormal distributions and spectra of solar wind plasma fluctuations: Wind 1995–1998. *J Geophys Res* **105**: 2357–2364. https://doi.org/10.1029/1999JA900442.

Cerisier JC, Berthelier JJ, Beghin C. 1985. Unstable density gradients in the high-latitude ionosphere. *Radio Sci* **20(4)**: 755–761. https://doi.org/10.1029/RS020i004p00755.

Chartier AT, Mitchell CN, Miller ES. 2018. Annual occurrence rates of ionospheric polar cap patches observed using Swarm. *J Geophys Res* **123(3)**: 2327–2335. https://doi.org/10.1002/2017JA024811.

Chernyshov AA, Chugunin DV, Frolov VL, Clausen LBN, Miloch WJ, et al. 2020. In situ observations of ionospheric heating effects: First results from a joint SURA and NorSat-1 experiment. *Geophys Res Lett* **47(13)**: e2020GL088462. https://doi.org/10.1029/2020GL088462.

Coley WR, Heelis RA. 1998. Seasonal and universal time distribution of patches in the northern and southern polar caps. *J Geophys Res* **103(A12)**: 29229–29237. https://doi.org/10.1029/1998JA900005.

Crowley G. 1996. Critical review of ionospheric patches and blobs. In: *Rev. Radio Sci. 1993–1996*, Ed. W.R., Stone, Oxford Science Publication, UK, pp. 619–648.

Crowley G, Carlson HC, Basu S, Denig WF, Buchau J, et al. 1993. The dynamic ionospheric polar hole. *Radio Sci* **28(3)**: 401–413. https://doi.org/10.1029/92RS02878.

Dandekar BS. 2002. Solar cycle dependence of polar cap patch activity. *Radio Sci* **37(1)**: 13-1–13-15. https://doi.org/10.1029/2000RS002562.

Dandekar BS, Bullett TW. 1999. Morphology of polar cap patch activity. *Radio Sci* **34(5)**: 1187–1205. https://doi.org/10.1029/1999RS900056.

Daniell R, Brown L. 1995. *Prism: A parameterized real-time ionospheric specification model, version 1.5*, Computational Physics Inc., Newton. Final report, 19 February 1992–31 March 1995.

Dyson PL, McClure JP, Hanson WB. 1974. In situ measurements of the spectral characteristics of F region ionospheric irregularities. *J Geophys Res (1896–1977)* **79(10)**: 1497–1502. https://doi.org/10.1029/JA079i010p01497.

Emmert JT, Richmond AD, Drob DP. 2010. A computationally compact representation of Magnetic-Apex and Quasi-Dipole coordinates with smooth base vectors. *J Geophys Res* **115(A8)**: A08322. https://doi.org/10.1029/2010JA015326.

Friis-Christensen E, Lühr H, Knudsen D, Haagmans R. 2008. Swarm – An Earth observation mission investigating geospace. *Adv Space Res* **41(1)**: 210–216. https://doi.org/10.1016/j.asr.2006.10.008.

Garner TW, Taylor BT, Gaussiran TL II, Coley WR, Hairston MR. 2005. On the distribution of ionospheric electron density observations. *Space Weather* **3(10)**: S10002. https://doi.org/10.1029/2005SW000169.

Hanson WB, Moffett RJ. 1966. Ionization transport effects in the equatorial F region. *J Geophys Res* **71(23)**: 5559–5572. https://doi.org/10.1029/JZ071i023p05559.

Heppner JP, Maynard NC. 1987. Empirical high-latitude electric field models. *J Geophys Res* **92(A5)**: 4467–4489. https://doi.org/10.1029/JA092iA05p04467.

Jin Y, Spicher A, Xiong C, Clausen LBN, Kervalishvili G, et al. 2019. Ionospheric plasma irregularities characterized by the Swarm satellites: Statistics at high latitudes. *J Geophys Res* **124(2)**: 1262–1282. https://doi.org/10.1029/2018JA026063.

Jin Y, Xiong C. 2020. Interhemispheric asymmetry of large-scale electron density gradients in the polar cap ionosphere: UT and seasonal variations. *J Geophys Res* **125(2)**: e2019JA027601. https://doi.org/10.1029/2019JA027601.

Jin Y, Xiong C, Clausen L, Spicher A, Kotova D, et al. 2020. Ionospheric plasma irregularities based on in situ measurements from the swarm satellites. *J Geophys Res* **125(7)**: e2020JA028103. https://doi.org/10.1029/2020JA028103.

Jin Y, Kotova D, Xiong C, Brask S, Clausen LBN, et al. 2022. Ionospheric Plasma IRregularities – IPIR – data product based on data from the Swarm satellites. *J Geophys Res* **127**: e2021JA030183. https://doi.org/10.1029/2021JA030183.

Jones GOL, Williams PJS, Winser KJ, Lockwood M. 1990. Characteristics of the high-latitude trough. *Adv Space Res* **10(6)**: 191–196. https://doi.org/10.1016/0273-1177(90)90253-V.

Kagawa A, Hosokawa K, Ogawa Y, Ebihara Y, Kadokura A. 2020. Occurrence distribution of polar cap patches: Dependences on UT, season and hemisphere. *J Geophys Res* **126(1)**: e2020JA028538. https://doi.org/10.1029/2020ja028538.

Karpachev AT, Gasilov NA, Karpachev OA. 2011. Morphology and causes of the Weddell Sea anomaly. *Geom Aeron* **51**: 812. https://doi.org/10.1134/s0016793211050070.

Kauristie K, Weygand J, Pulkkinen TI, Murphree JS, Newell PT. 1999. Size of the auroral oval: UV ovals and precipitation boundaries compared. *J Geophys Res* **104(A2)**: 2321–2331. https://doi.org/10.1029/1998JA900046.

Laundal KM, Cnossen I, Milan SE, Haaland SE, Coxon J, et al. 2017. North-South asymmetries in Earth's magnetic field. *Space Sci Rev* **206(1)**: 225–257. https://doi.org/10.1007/s11214-016-0273-0.

Laundal KM, Østgaard N. 2009. Asymmetric auroral intensities in the Earth's Northern and Southern hemispheres. *Nature* **460 (7254)**: 491–493. https://doi.org/10.1038/nature08154.

Lin CH, Liu JY, Cheng CZ, Chen CH, Liu CH, et al. 2009. Three-dimensional ionospheric electron density structure of the Weddell Sea Anomaly. *J Geophys Res* **114(A2)**: A02312. https://doi.org/10.1029/2008JA013455.

Lorentzen DA, Shumilov N, Moen J. 2004. Drifting airglow patches in relation to tail reconnection. *Geophys Res Lett* **31(2)**: L02806. https://doi.org/10.1029/2003GL017785.

Noja M, Stolle C, Park J, Lühr H. 2013. Long-term analysis of ionospheric polar patches based on CHAMP TEC data. *Radio Sci* **48(3)**: 289–301. https://doi.org/10.1002/rds.20033.

Østgaard N, Laundal KM, Juusola L, Åsnes A, Håland SE, et al. 2011. Interhemispherical asymmetry of substorm onset locations and the interplanetary magnetic field. *Geophys Res Lett* **38(8)**. https://doi.org/10.1029/2011GL046767.

Pal M, Ali MM, Woo J. 2006. Exponentiated Weibull distribution. *Statistica* **66(2)**: 139–147. https://doi.org/10.6092/issn.1973-2201/493.

Palmroth M, Grandin M, Sarris T, Doornbos E, Tourgaidis S, et al. 2021. Lower-thermosphere–ionosphere (LTI) quantities: current status of measuring techniques and models. *Ann Geophys* **39(1)**: 189–237. https://doi.org/10.5194/angeo-39-189-2021.

Park J, Lühr H, Min KW. 2010. Neutral density depletions associated with equatorial plasma bubbles as observed by the CHAMP satellite. *J Atmos Sol-Terr Phys* **72(2)**: 157–163. https://doi.org/10.1016/j.jastp.2009.11.003.

Ren J, Zou S, Gillies RG, Donovan E, Varney RH. 2018. Statistical characteristics of polar cap patches observed by RISR-C. *J Geophys Res* **123(8)**: 6981–6995. https://doi.org/10.1029/2018JA025621.

Richmond AD. 1995. Ionospheric electrodynamics using magnetic apex coordinates. *J Geomag Geoelectr* **47**: 191. https://doi.org/10.5636/jgg.47.191.

Rodger A, Graham A. 1996. Diurnal and seasonal occurrence of polar patches. *Ann Geophys* **14(5)**: 533–537. https://doi.org/10.1007/s00585-996-0533-5.

Rodger AS, Pinnock M, Dudeney JR, Baker KB, Greenwald RA. 1994. A new mechanism for polar patch formation. *J Geophys Res* **99(A4)**: 6425–6436. https://doi.org/10.1029/93JA01501.

Sarris TE, Talaat ER, Palmroth M, Dandouras I, Armandillo E, et al. 2020. Daedalus: a low-flying spacecraft for in situ exploration of the lower thermosphere–ionosphere. *Geosci Instrum Method Data Syst* **9(1)**: 153–191. https://doi.org/10.5194/gi-9-153-2020.

Schunk RW, Scherliess L, Sojka JJ, Thompson DC, Anderson DN, et al. 2004. Global assimilation of ionospheric measurements (GAIM). *Radio Sci* **39(1)**: RS1S02. https://doi.org/10.1029/2002RS002794.

Seguro JV, Lambert TW. 2000. Modern estimation of the parameters of the Weibull wind speed distribution for wind energy analysis. *J Wind Eng Ind Aerodyn* **85(1)**: 75–84. https://doi.org/10.1016/S0167-6105(99)00122-1.

Silva EL, Lisboa P. 2007. Analysis of the characteristic features of the density functions for gamma, Weibull and log-normal distributions through RBF network pruning with QLP. In: *Presented at the Proceedings of the 6th Conference on 6th WSEAS Int. Conf. on Artificial Intelligence, Knowledge Engineering and Data Bases – Volume 6*, Corfu Island, Greece, February 16–19, 2007, pp. 223–228.

Smith J, Heelis RA. 2017. Equatorial plasma bubbles: Variations of occurrence and spatial scale in local time, longitude, season, and solar activity. *J Geophys Res* **122(5)**: 5743–5755. https://doi.org/10.1002/2017JA024128.

Spicher A, Clausen LBN, Miloch WJ, Lofstad V, Jin Y, et al. 2017. Interhemispheric study of polar cap patch occurrence based on Swarm in situ data. *J Geophys Res* **122(3)**: 3837–3851. https://doi.org/10.1002/2016JA023750.

Spogli L, Sabbagh D, Regi M, Cesaroni C, Perrone L,. 2020. Ionospheric response over Brazil to the August 2018 geomagnetic storm as probed by CSES-01 and Swarm satellites and by local ground-based observations. *J Geophys Res* **126(2)**: e2020JA028368. https://doi.org/10.1029/2020JA028368.

Tindale E, Chapman SC. 2017. Solar wind plasma parameter variability across solar cycles 23 and 24: From turbulence to extremes. *J Geophys Res* **122(10)**: 9824–9840. https://doi.org/10.1002/2017JA024412.

Turel N, Arikan F. 2010. Probability density function estimation for characterizing hourly variability of ionospheric total electron content. *Radio Sci* **45(6)**: RS6016. https://doi.org/10.1029/2009RS004345.

Woodman RF, La Hoz C. 1976. Radar observations of F region equatorial irregularities. *J Geophys Res* **81(31)**: 5447–5466. https://doi.org/10.1029/JA081i031p05447.

Yang YY, Zhima ZR, Shen XH, Chu W, Huang JP, et al. 2020. The first intense geomagnetic storm event recorded by the China Seismo-Electromagnetic Satellite. *Space Weather* **18(1)**: e2019SW002243. https://doi.org/10.1029/2019SW002243.

Zhang QH, Zhang YL, Wang C, Oksavik K, Lyons LR, et al. 2021. A space hurricane over the Earth's polar ionosphere. *Nat Commun* **12(1)**: 1207. https://doi.org/10.1038/s41467-021-21459-y.